

# Oxygen-rich semiregular and irregular variables\*

## A catalogue of circumstellar CO observations

F. Kerschbaum<sup>1,2</sup> and H. Olofsson<sup>2</sup>

<sup>1</sup> Institut für Astronomie, Türkenschanzstraße 17, A-1180 Wien, Austria

<sup>2</sup> Stockholms Observatorium, SE-13336 Saltsjöbaden, Sweden

Received February 25; accepted June 4, 1999

**Abstract.** Using the SEST, the Onsala 20 m telescope, the JCMT, and the IRAM 30 m telescope we have carried out a survey of circumstellar CO( $J = 1 - 0$ ,  $2 - 1$ ,  $3 - 2$ , and  $4 - 3$ ) emission on a large sample of oxygen-rich semiregular (SRa and SRb) and irregular variables (Lb). A total of 109 stars were observed in at least one CO line: 66 were shown to have circumstellar CO line emission (7 SRa, 36 SRb, and 23 Lb variables),  $\sim 60\%$  of the semiregulars and all but one of the irregulars were detected for the first time. Most stars were observed in at least two transitions. There is a total of 138 detected CO lines. For twelve stars strong interference from interstellar CO emission precluded detection.

We present here a catalogue of all observational data and the spectra of all detections, as well as brief discussions on detection statistics (including its dependence on variability type, period, IRAS-colour, IRAS LRS-class, and M-subclass), line profiles (including line shape asymmetry, multi-component line shapes, and line intensity ratios), gas expansion velocity distributions, and correlations between CO line and IR continuum fluxes (including implications for the mass-loss mechanism).

**Key words:** stars: variables: general — stars: AGB and post-AGB — stars: circumstellar matter — stars: mass-loss — radio lines: stars

## 1. Introduction

Circumstellar CO radio line emission has proven to be a good measure of the gas mass-loss rate of evolved stars on the Asymptotic Giant Branch (AGB). Extensive surveys have been performed, and presently more than 500 objects have been detected (e.g., Knapp & Morris 1985; Zuckerman & Dyck 1986; Zuckerman et al. 1986; Leahy et al. 1987; Nguyen-Q-Rieu et al. 1986; Knapp et al. 1989; Loup et al. 1990; Margulis et al. 1990; Likkell et al. 1991; Bujarrabal et al. 1992; Nyman et al. 1992; Kastner et al. 1993; Olofsson et al. 1993; van der Veen et al. 1993; Volk et al. 1993; Bieging & Latter 1994; Hu et al. 1994; Kahane & Jura 1994; Sahai & Liechti 1995; Young 1995; Groenewegen et al. 1996; Kerschbaum et al. 1996c; Bieging et al. 1998; Groenewegen & de Jong 1998; Josselin et al. 1998; Knapp et al. 1998; Kerschbaum & Olofsson 1998). A significant fraction of this work was catalogued by Loup et al. (1993, hereafter L93). The surveys are dominated by high mass-loss rate, evolved objects. The low end of the mass-loss rate distribution, populated by objects located on the early AGB or at the beginning of the thermally pulsing AGB (i.e., the phase of episodic double-shell burning), has not been studied in that detail. We therefore started a major survey of circumstellar CO emission towards cool, O-rich ( $O/C > 1$ ) semiregular (SRVs) and irregular (IRVs) variables.

The SRVs (types SRa and SRb) and the IRVs (Lb) are quite numerous groups of objects among the stars on the AGB. They can provide important constraints for theoretical mass-loss models due to their different pulsational behaviour compared to the more frequently studied Mira variables. In a series of papers (Kerschbaum & Hron 1992, 1994, 1995, hereafter SR\_I, SR\_IIa, and SR\_III, respectively; Kerschbaum 1995, hereafter SR\_IIb) the SRVs have been studied in a broad and systematic way. This made it possible to divide this inhomogeneous group of objects into physically distinct classes, based on stellar properties and galactic distribution. For the O-rich stars

---

Send offprint requests to: F. Kerschbaum,  
Internet: kerschbaum@astro.univie.ac.at

\* Based on observations collected using at the European Southern Observatory, La Silla, Chile, the Onsala Space Observatory, Chalmers Tekniska Högskola, Sweden, the James Clerk Maxwell Telescope, Hawaii and the IRAM 30 m telescope, Pico Veleta, Spain.

the subclasses “blue”-, “red”-, and “Mira”-SRVs were introduced. The “blue” subclass contains objects with short periods (typically below  $100^d$ ) and no apparent signs of mass-loss. The border between “red”- and “Mira”-SRVs is mainly defined by the period ( $P < 200^d$  for “red”, and  $P > 200^d$  for “Mira”). The “blue”-SRVs seem to be on the early AGB, while the other two groups are on the thermally pulsing AGB. Jura & Kleinmann (1992) reached the same conclusions concerning the galactic distribution of these stars.

Work on the IRVs is complicated by the larger contamination by poorly observed late-type variables (to some extent this applies also to the SRVs, Lebzelter et al. 1995). Kerschbaum et al. (1996b, hereafter Lb\_I) found that their sample of visually bright IRVs displays infrared properties very similar to the SRVs. There may be a slightly larger “contamination” with non-AGB giants than in the case of the SRVs, but the AGB objects seem to resemble the “blue” and the “red” SRVs. In a paper by Kerschbaum et al. (1996a) based on NIR- and IRAS-photometry, full spectral energy distributions, mass-loss rates, and galactic distributions were analyzed, and the similarity between the IRVs and SRVs was further demonstrated.

A more detailed study of the circumstellar properties of O-rich SRVs started with the work of Kahane & Jura (1994, hereafter K94) who published high quality CO ( $J = 1 - 0$  and  $2 - 1$ ) line observations of eleven nearby objects. They came to the conclusion that these objects have mass-loss properties quite similar to those of longer-period O-rich Miras. Kerschbaum et al. (1996c, hereafter SR\_IV) extended this work considerably in their study of O-rich SRVs. The majority of their detected objects, covering both small and longer periods, are low mass-loss rate objects ( $\lesssim 10^{-7} M_{\odot} \text{ yr}^{-1}$ ), and low expansion velocity envelopes (the mean value is  $\sim 8 \text{ km s}^{-1}$ ). A significant number of C-rich SRVs and IRVs was included in the survey of Olofsson et al. (1993).

O-rich IRVs were for the first time studied in circumstellar CO by Kerschbaum & Olofsson (1998). They found that their mass-loss properties are very similar to those of O-rich SRVs and (optically bright) Miras, i.e., at least in this mass-loss rate range the stellar mass-loss properties are not strongly influenced by the pulsational behaviour of the star.

In this paper we present a catalogue and spectra of all CO radio line data that we have obtained towards O-rich SRVs and IRVs. In total 66 sources have been detected, 43 SRVs and 23 IRVs. Only a minor fraction of the data have already been presented in Kerschbaum et al. (1996c) and Kerschbaum & Olofsson (1998). We also discuss some of the quantitative results that can be derived directly from the data.

## 2. Observations

The CO ( $J = 1 - 0, 2 - 1, 3 - 2, 4 - 3$ ) observations presented in this paper were carried out in the years 1993 to 1998. The long time span and the varying availability of receivers have led to some selection effects and different completeness levels in this catalogue. Statistical consequences are discussed in Sect. 3. Here we give the basic criteria for the sample selection, describe the instruments used, and present the observational results.

### 2.1. The sample

A number of well studied O-rich SRa and SRb variables were selected on the basis of their IRAS-60  $\mu\text{m}$  flux densities (typically  $S_{60} \geq 5 \text{ Jy}$ ). As expected from the small dust mass-loss rates (SR\_I) only very few of the objects were already detected in CO radio lines before our survey started (L93; K94). Our first results were published in SR\_IV. Subsequently, these observations have been supplemented by observations of additional sources and additional transitions for already detected objects.

We selected the O-rich IRVs also on the basis of their IRAS-60  $\mu\text{m}$  flux densities, but down to levels of about 2 Jy in order to get a comparable number of IRVs and SRVs. Nothing was known about their circumstellar CO properties before we started this survey. Based on our experience with the SRVs (SR\_IV) only objects redder than 0.36 in the zero-point corrected IRAS-colour  $[12 \mu\text{m}] - [25 \mu\text{m}]^1$  were observed in order to save observing time. This biased our sample towards mass losing objects with properties similar to those of “red” and “Mira”-SRVs. First results on these observations have been published in Kerschbaum & Olofsson (1998).

In the appendix Tables A1 and A2 list basic properties of the observed stars. Among others the source of the listed coordinates (GCVS4 = General Catalogue of Variable Stars, 4<sup>th</sup> edition, GSC = Guide Star Catalog, HIC = Hipparcos Input Catalogue, Sim = Simbad, TYC = Tycho Catalogue) is given. Most coordinates are of sub-arcsecond accuracy. In the few cases where only GCVS4 coordinates were available the quality was checked against the IRAS-PSC coordinates. The periods listed originate from the GCVS4.

Table 1 gives the number of stars,  $n_{\text{star}}$ , in our sample down to a given  $S_{60}$  level and divided into the variability groups.

### 2.2. The observing runs

The observations in the CO ( $J = 1 - 0$ ) line were obtained using the Swedish-ESO Submillimetre Telescope (SEST),

<sup>1</sup> To convert our zero corrected colours to the originally not corrected ones  $1^m56$  and  $1^m88$  has to be subtracted from  $[12 \mu\text{m}] - [25 \mu\text{m}]$  and  $[25 \mu\text{m}] - [60 \mu\text{m}]$ , respectively.

**Table 1.** Statistics on observations and detections

$S_{60}(\text{Jy}) \geq$	$n_{\text{star}}$			$n_{\text{obs}}$			$n_{\text{det}}$			$n_{\text{det}}/n_{\text{obs}}$ (%)			$n_{\text{obs}}/n_{\text{star}}$ (%)		
	10	5	2	10	5	2	10	5	2	10	5	2	10	5	2
Lb	10	28	70	6	22	37	4	13	22	67	59	59	60	79	53
SRa	8	15	33	8	15	15	3	7	7	38	47	47	100	100	46
SRb	45	76	141	41	52	57	32	36	37	78	69	64	91	68	40

**Table 2.** Data on Telescopes and Receivers

Telescope	Frequency	Beamwidth	$T_{\text{rec}}$	$\eta_{\text{mb}}$
IRAM	115271 MHz	22''	100 K	0.72
IRAM	230537 MHz	11''	120 K	0.45
JCMT	230537 MHz	21''	180 K	0.71
JCMT	345796 MHz	13''	200 K	0.60
JCMT	461041 MHz	11''	550 K	0.53
OSO	115271 MHz	33''	150 K	0.50
SEST	115271 MHz	45''	130 K	0.70
SEST	230537 MHz	23''	150 K	0.50
SEST	345796 MHz	16''	350 K	0.25

Chile, the 20 m telescope at Onsala Space Observatory (OSO), Sweden, and the IRAM 30 m telescope, Spain. The CO ( $J = 2 - 1$ ) data were obtained at the SEST, the James Clerk Maxwell Telescope (JCMT), Hawaii, and the IRAM telescope. The CO ( $J = 3 - 2, 4 - 3$ ) data were obtained with the JCMT. The observing runs at SEST were made in January 1993, August 1994, December 1996, and August 1998. In March 1994 and 1995, and February 1997 we had observing runs at OSO. JCMT was used in flexible scheduling mode, or in backup programme mode, during the observing periods 96B, 97A and 97B. The IRAM spectra were obtained in April 1997. Telescope and receiver data are given in Table 2.  $T_{\text{rec}}$  and  $\eta_{\text{mb}}$  stand for the representative noise temperature of the receiver (SSB) and the main beam efficiency of the telescope, respectively.

As spectrometers we used 1 MHz filterbanks at IRAM, an autocorrelation spectrometer at the JCMT (250 MHz bandwidth with 160 kHz channel separation), 2 filterbanks at OSO ( $256 \times 250$  kHz, and  $512 \times 1$  MHz), and 3 acousto-optical spectrometers at SEST (86 MHz bandwidth with 43 kHz channel separation, 500 MHz bandwidth with a 0.7 MHz channel separation, and 1 GHz bandwidth with 0.7 MHz channel separation). At IRAM and at the JCMT beam switching (2') with a chopping secondary was used. Dual beam switching (beam throws of about 10'), in which the source was placed alternately in the two beams, was used to eliminate baseline ripples at OSO and SEST. All data were calibrated by the chopper-wheel method, and the intensity scale is given in terms of main beam brightness temperature,  $T_{\text{mb}}$ .

### 2.3. Observational results

A total of 109 stars were observed in at least one CO line: 66 were shown to have circumstellar CO line emission (7 SRa, 36 SRb, and 23 Lb variables),  $\sim 60\%$  of the SRVs and all but one of the IRVs were detected for the first time. Most stars were observed in at least two transitions. There is a total of 138 detected CO lines. For twelve stars any possible detections were precluded because of strong interference from interstellar CO emission.

Table 1 gives our detection statistics. All numbers are given for three selection limits in  $S_{60}$ .  $n_{\text{star}}$  stands for the total number of stars in the GCVS4 down to the given  $S_{60}$ .  $n_{\text{obs}}$  is the number of stars observed in CO by us.  $n_{\text{det}}$  gives the number of detected sources (not transitions!).  $n_{\text{det}}/n_{\text{obs}}$  and  $n_{\text{obs}}/n_{\text{star}}$  give the detection rate and the fraction of the sample observed in percent, respectively. About 75% of all Lbs, SRAs and SRBs have now been observed down to an  $S_{60}$  level of 5 Jy.

Tables A3–A8 in the appendix list all our observations. The names in the GCVS4 and the IRAS-PSC are given. The first letter of the code denotes the observatory (IRAM, JCMT, OSO, or SEST), the rest the transition observed. Another code reflects the “success” of the observation (Detection, Non-detection, Tentative detection). An “i” indicates contamination by interstellar CO lines.

When determining the line parameters we compared the results of fitting parabolas or 4<sup>th</sup> order polynomials, which generally fit the lines very well, with eye estimates of where the profiles go to zero intensity. There was in general a good agreement between the results obtained with the two methods. We determined the zero intensity velocities (i.e., the velocities at the two edges of the line profile) from the best fits. The stellar velocity was then derived from the average and the gas expansion velocity of the envelope from half the difference between these velocities, respectively. Before doing this we removed the major baseline irregularities by fitting low order polynomials to the spectra. We estimate that both quantities are uncertain by about 1 – 2 km s<sup>-1</sup>, but the uncertainty varies with the S/N-ratio. This means that the low expansion velocities may be uncertain by up to 30%, while for the highest expansion velocities the uncertainty decreases to about 10%. The stellar velocity is given with respect to the heliocentric ( $v_{\text{hel}}$ ) and the LSR frame [ $v_{\text{LSR}}$ ; the Local Standard of Rest is defined using standard solar motion (B1950.0):  $v_{\odot} = 20 \text{ km s}^{-1}$ ,  $\alpha_{\odot} = 270^{\circ}5$ ,  $\delta_{\odot} = +30^{\circ}0$ ].

The peak main beam brightness temperature,  $T_{\text{mb}}$ , is obtained as an average of the line profile intensities in the velocity range  $v_{\text{hel}} \pm 0.2v_{\text{exp}}$ . The integrated intensity,  $I = \int T_{\text{mb}} dv$ , is obtained by integrating the line intensities over the velocity range  $v_{\text{hel}} \pm v_{\text{exp}}$ . Once again the uncertainty in both quantities varies with the S/N-ratio, but we estimate that it is on average 24% in  $T_{\text{mb}}$ , 12% in  $I$ , and in the worst cases it may reach 50% in both quantities. To this should be added an estimated uncertainty in the absolute calibration of about 20%. For a non-detection an upper limit to  $I$  is estimated by measuring the peak-to-peak noise ( $T_{\text{pp}}$ ) of the spectra with a velocity resolution reduced to  $15 \text{ km s}^{-1}$  and calculating  $I = 15T_{\text{pp}}$ . The Q-column gives a quality ranking: 5 (non-detection), 4 (tentative detection, or detection with very low S/N-ratio  $\lesssim 3$ ), 3 (detection, low S/N-ratio  $\approx 5$ ), 2 (detection, good S/N-ratio  $\approx 10$ ), and 1 (detection, very good S/N-ratio  $\gtrsim 15$ ). The S/N-ratio given is in terms of peak main beam brightness temperature divided by the 1 sigma noise for typical cases. A spectrum must have quality 3 or better to be used in the analysis. Finally, in cases of complex velocity profiles the measured component C is indicated in the form **b**=broad, **n**=narrow, **b+n**=total.

All spectra are shown in Figs. A1 to A7. Their order differ from that in Tables A3–A8, where the ordering is based on the source coordinates. Since we have a sample of visually bright variables we use the GCVS4-name to order the stars in figures. Tables A3–A8 allow the reader to identify the GCVS4-name if only the IRAS-name or the coordinates are known. The velocity scale is given in the heliocentric system (Tables A3–A8 list the corresponding LSR velocities). The velocity resolution is reduced to  $1 \text{ km s}^{-1}$ , except for some low S/N-ratio spectra where a resolution of  $2 \text{ km s}^{-1}$  or even  $4 \text{ km s}^{-1}$  is used.

As expected from our earlier work we find no significant differences in the behaviour of the SRVs and IRVs in most of the studied properties. Consequently, they are combined in a large fraction of the figures in this paper.

### 3. Detectability

#### 3.1. Variability type

As shown in Table 1 the  $n_{\text{det}}/n_{\text{obs}}$  value differs somewhat between the three variability groups (59% for the Lbs, 47% for SRAs, and 64% for SRbs). This does not necessarily have a physical reason, but may be due to a selection effect. The relatively low value for the SRA variables (the smallest group) is probably due to the fact that we tried to observe all objects down to the  $S_{60}$ -limit, whereas in the cases of the SRbs and the Lbs we avoided observations of “blue”-objects (see below), and objects with very short periods. Consequently, any statistics derived from these observations has to be very preliminary until we arrive at more complete samples, but at this stage we find

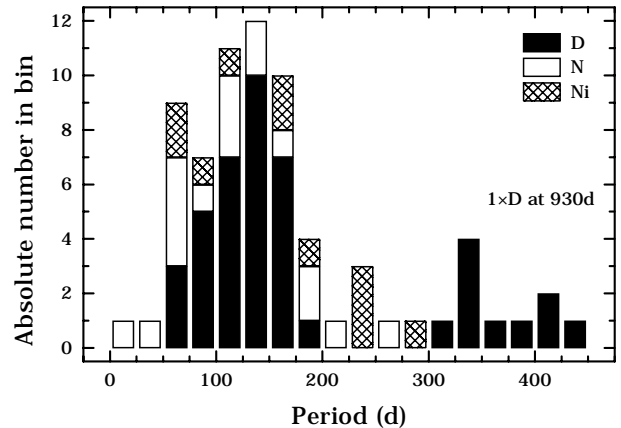


Fig. 1. Period distribution of the observed SRVs. The different shadings denote the success of detection

no differences between the “reddened” IRVs and SRVs in terms of CO detectability. The total detection rates are high, 71% for the 10 Jy-limit, 63% for the 5 Jy-limit and decreasing only marginally to 61% for all observations.

#### 3.2. Period

In Fig. 1 we present the detection rate as a function of the period for the SRVs. The statistics is poor in some period ranges, but it appears that the detection rate decreases for the shorter periods ( $\lesssim 75^{\text{d}}$ ), that it is hard to detect stars in the intermediate period range ( $200^{\text{d}} - 300^{\text{d}}$ , although the fraction of stars with interstellar CO confusion is high here), while for the longer periods ( $> 300^{\text{d}}$ ) the detection rate approaches 100%. For the Miras observed by Young (1995, Y95) the detection rate drops drastically when going to periods shorter than  $325^{\text{d}}$  (from about 70% to 30%), i.e., a very similar behaviour. Since we do not expect large luminosity differences among our stars (i.e., the sampled volume does not depend on the period), our detection statistics should be mainly caused by differences in mass-loss rate.

#### 3.3. IRAS-colour

In Fig. 2 we have plotted all our observed stars in the classical IRAS two-colour diagram (van der Veen & Habing 1988; including the regions introduced by them). There is no apparent trend in the detection rate with far-infrared colour, except that the six “bluest” SRVs, located in region I, were not detected. For Lbs no objects bluer than 0.36 in  $[12 \mu\text{m}] - [25 \mu\text{m}]$  were observed. Our sample objects populate, as expected, mainly regions II and IIIa. We note that the fraction of stars where the spectra are confused by interstellar CO emission increases with redder  $[12 \mu\text{m}] - [25 \mu\text{m}]$  and  $[25 \mu\text{m}] - [60 \mu\text{m}]$  colours, suggesting that the IRAS fluxes are not entirely free from an interstellar contribution.

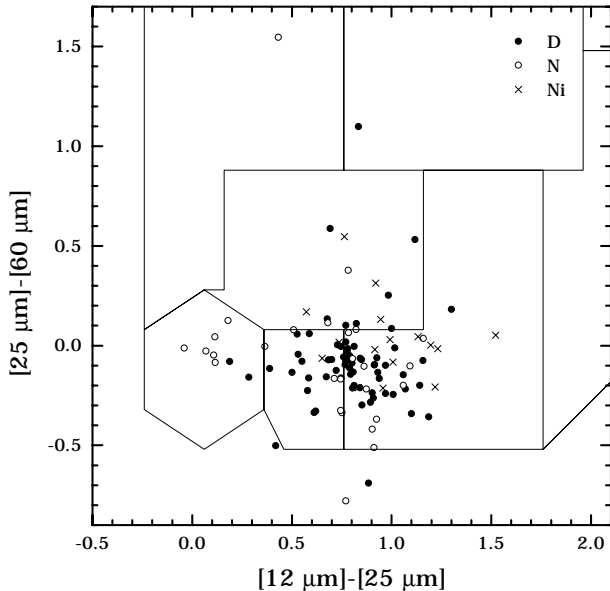


**Fig. 2.** IRAS two-colour diagram for the observed stars. The different symbols denote the success of detection

### 3.4. IRAS LRS-class and M-subclass

The IRAS LRS-class is an independent quantity measuring dust mass-loss in a qualitative sense. Figure 3 gives the detection statistics for the IRAS LRS-classes. No clear trend is visible. We detect objects with a silicate emission feature ( $2n$  class) as well as without a clear feature (the latter sources showing only a “flat” continuum, LRS-classes 14 – 17). However, from recent ISO results (e.g., Kerschbaum et al. 1997) we have indication that many  $1n$ -class objects show another dust feature at  $13 \mu\text{m}$ , normally attributed to corundum (crystalline  $\text{Al}_2\text{O}_3$ , e.g. Begemann et al. 1997). Generally, one finds a stronger  $13 \mu\text{m}$  feature for the warmer objects, whereas the colder ones are dominated by broad silicate emission at 10 and  $18 \mu\text{m}$ .

Figure 4 gives the detection statistics for the M-subclasses. There is a trend of increasing detection rate with increasing sub-class (hence decreasing temperature), although we have very few objects with early and late sub-classes. This again is comparable to the results on Miras by Y95.

Consequently, the detectability appears not to be very affected by the composition of the circumstellar dust or the stellar atmospheric temperature. However, we are still dealing with a small sample of objects, where we have concentrated on those expected to have circumstellar envelopes.

## 4. Line profiles

### 4.1. Line shapes

Within the limitations of the S/N-ratio most of the line profiles lie in the range of the expected, i.e., between a

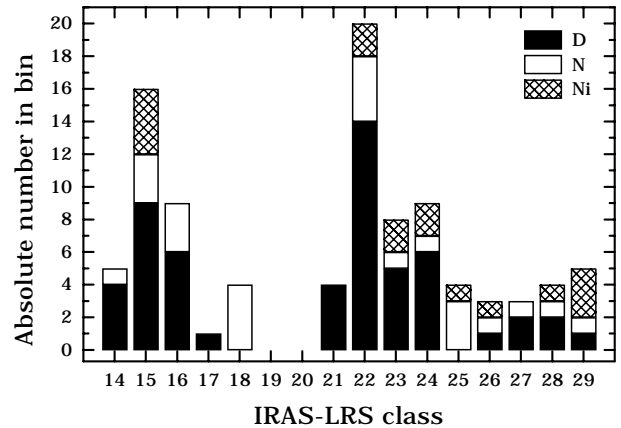


**Fig. 3.** IRAS LRS-class distribution of the observed stars. The different shadings denote the success of detection

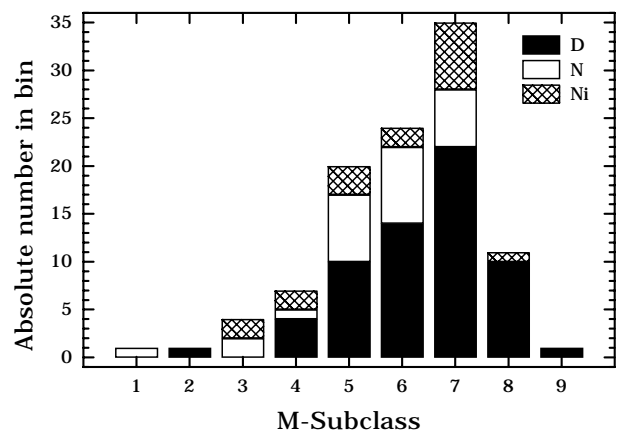


**Fig. 4.** Spectral M-subclass distribution of the observed stars. The different shadings denote the success of detection

rectangular (spatially unresolved, optically thin emission) and a parabolic (spatially unresolved, optically thick emission) line shape. Nevertheless, there is a relatively high fraction of lines showing various kinds of asymmetry. In a few cases the line shapes clearly suggest the presence of at least two winds with different velocities.

#### 4.1.1. Asymmetry

We have calculated a simple line asymmetry factor,  $I_{r/b}$ , for the lines with the highest S/N-ratios, see Tables A3–A8. It gives the ratio of the integrated intensities on the red- and blue-shifted sides of the central velocity (determined by a fit, see Sect. 2.3). The results are given in Fig. 5. It is clear that the lines are on average stronger on the red-shifted side, but the asymmetry decreases with increasing excitation requirements for the transition (note the markedly lower number of high-quality  $1-0$  spectra due to the relative weakness of this line). The mean (median) values for the  $1-0$ ,  $2-1$ , and  $3-2$  lines are 1.13 (1.16), 1.10 (1.09), and 1.03 (1.03), respectively. A straightforward explanation to the asymmetry is

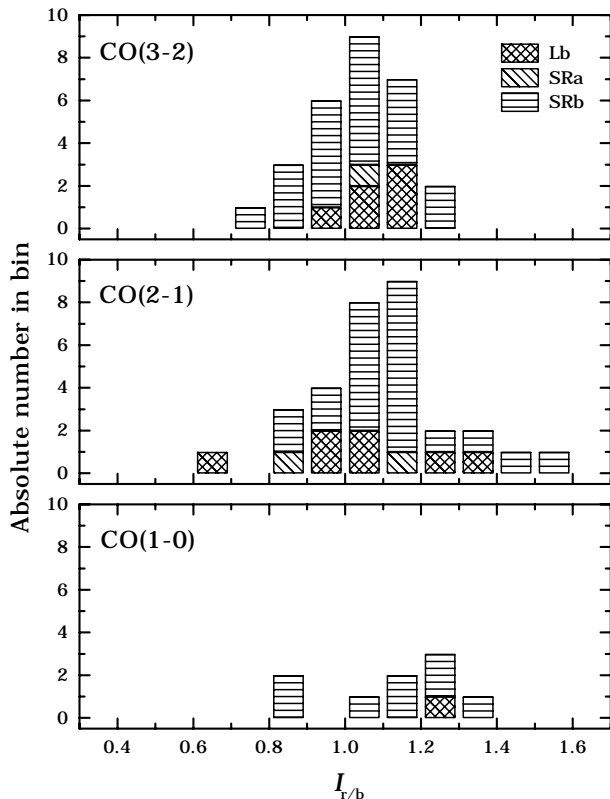


**Fig. 5.** Distribution of the asymmetry parameter  $I_{r/b}$  for the CO ( $J = 1 - 0$ ,  $2 - 1$ , and  $3 - 2$ ) lines

self-absorption in an envelope with a negative radial temperature gradient (as first observed in IRC+10216 by Olofsson et al. 1982, and modelled by Huggins & Glassgold 1986). The trend with  $J$ -level probably reflects the fact that the higher- $J$  lines come from regions closer to the star where self-absorption is less important.

#### 4.1.2. Multi-component line profiles

Among our detected stars there are four that clearly show multi-component line profiles: EP Aqr, RV Boo, X Her, and SV Psc (all are SRBs). Typically a very narrow feature with a full width less than  $\sim 5 \text{ km s}^{-1}$  is centered, within the uncertainties, on a much broader line  $\sim 18 \text{ km s}^{-1}$ , see Table 3. The broad component is close to being parabolic. SV Psc and EP Aqr are maybe the most extreme examples of this phenomenon. The central peaks are very narrow, and, if interpreted as arising from expanding envelopes, they imply expansion velocities of  $\sim 2 \text{ km s}^{-1}$ . In RV Boo, the only one of these stars for which we have high-quality data in two lines, the narrow component becomes much stronger (relative to the broad component) for the higher-frequency transition. Knapp et al. (1998) recently presented and discussed similar data for nine stars.

One possible interpretation of these observations is outlined in Kahane & Jura (1996) where they reported

on a bipolar outflow around the nearby X Her. They were able to spatially resolve the blue- and red-shifted lobes of a (weakly collimated) bipolar outflow, while the low-velocity emission, i.e., the narrow component, appears to outline a symmetric envelope. In the case of RV Boo we have obtained data with the OVRO mm-wave interferometer, which partly resolved the CO(2-1) emission from this more distant object. The data suggest that in this case it is rather the narrow component that originates from a bipolar outflow, while the higher-velocity gas comes from a symmetric envelope. However, a final interpretation has to await a more detailed analysis. Knapp et al. (1998), on the other hand, suggest a scenario where episodic mass-loss plays a role.

A similar narrow spike in the middle of a broader line could also be interpreted in terms of emission from a long-lived disk as suggested by Jura et al. (1995) for the post-AGB object the Red Rectangle, and by Kahane et al. (1998) for the “silicate” carbon star BM Gem.

At this stage no definite conclusions can be drawn, except that it is very likely that these objects are far off the picture of a constant, spherically symmetric mass-loss.

#### 4.2. Gas expansion velocities

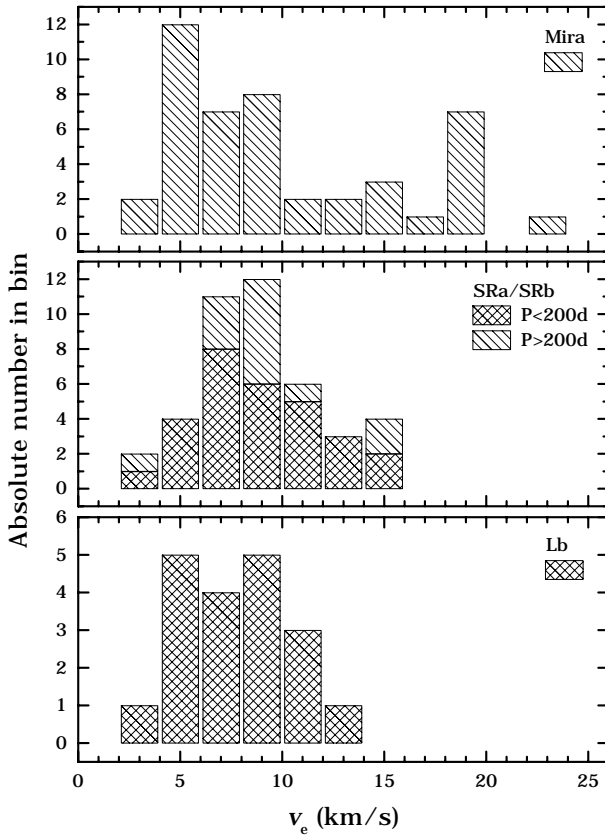
In this section we compare the circumstellar gas expansion velocities obtained from our data on the SRVs and IRVs with results taken from the literature for O-rich Mira variables (L93; Y95). The two sources for the Mira data differ significantly in their selection criteria. Whereas L93 contains a very inhomogeneous collection from many different surveys, Y95 is a distance limited survey of visually bright Miras, i.e., an approach that is quite similar to ours. However, since only visually classified Miras (GCVS4) were taken from L93, also this data set provides us with stars of comparable properties. Finally, we note here that one expects only small systematic errors in the gas expansion velocity estimates between different studies, as opposed to the case for the mass-loss rate. If, for an individual object, more than one independent measurement of  $v_e$  are available the best was chosen, or, if they are of comparable quality, they were averaged. The resulting gas expansion velocity distributions are shown in Fig. 6.

The mean (median) velocities for the three sub-samples are  $7.7$  ( $7.9$ )  $\text{km s}^{-1}$  (IRV),  $8.8$  ( $8.3$ )  $\text{km s}^{-1}$  (SRV), and  $10.0$  ( $8.6$ )  $\text{km s}^{-1}$  (Mira). The main difference between the groups is the existence of a tail towards high expansion velocities among the Miras. These are all longer-period Miras as can be seen in Fig. 7. Of particular interest for mass-loss mechanism discussions is the high number of stars, in all three groups, with very low expansion velocities,  $v_e \lesssim 5 \text{ km s}^{-1}$ . We here just mention a few clear examples from our data: the IRVs V584 Aql, BI Car, and AZ UMa; the SRVs T Ari, RX Lep, L<sup>2</sup> Pup, Y Tel, and

**Table 3.** Multi-component line profiles<sup>a</sup>

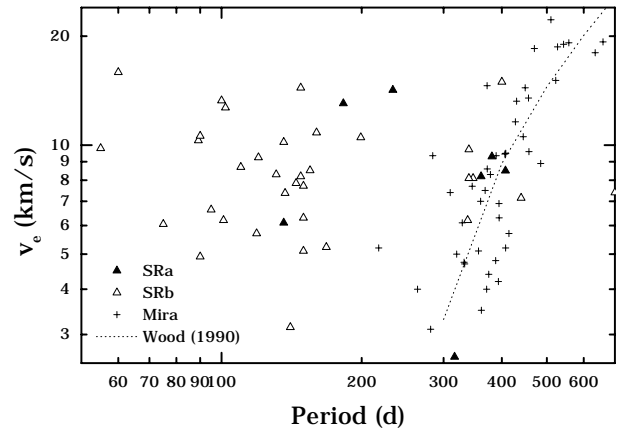
		narrow			broad		
		$v_{\text{hel}}$ km s <sup>-1</sup>	$v_e$ km s <sup>-1</sup>	$I$ Kkm s <sup>-1</sup>	$v_{\text{hel}}$ km s <sup>-1</sup>	$v_e$ km s <sup>-1</sup>	$I$ Kkm s <sup>-1</sup>
EP Aqr	1-0, SEST	-43.1	1.5	0.72	-43.1	10.7	4.9
RV Boo	2-1, JCMT	-6.3	2.7	0.84	-6.5	8.1	3.7
	3-2, JCMT	-6.2	2.8	2.1	-7.0	8.4	5.0
X Her	3-2, JCMT	-90.6	3.1	8.3	-90.5	8.0	18.2
SV Psc	2-1, SEST	10.2	2.3	0.48	10.4	10.8	1.5

<sup>a</sup> The velocities and intensities are obtained from fits of parabolas to the narrow and broad components separately.


**Fig. 6.** Distribution of circumstellar gas expansion velocities

BK Vir. The median values obtained for this sample of O-rich IRVs and SRVs are clearly lower than the corresponding values obtained by Olofsson et al. (1993) for a sample of optically bright carbon stars,  $10.5 \text{ km s}^{-1}$  and  $10.8 \text{ km s}^{-1}$ , respectively, and in the latter sample (68 objects) there are only two objects with expansion velocity estimates below  $5 \text{ km s}^{-1}$ .

In Fig. 7 we have plotted the gas expansion velocity as a function of the pulsation period for our SRV sample and the Miras. For SRVs below periods of about 200 days there appears to be no trend in the expansion velocity. For longer periods ( $\gtrsim 300^{\text{d}}$ , i.e., in the classical Mira regime) it seems that the expansion velocity increases with period in the way suggested by Wood (1990, dotted line in Fig. 7), although there is a considerable scatter. It is


**Fig. 7.** Gas expansion velocity versus the pulsation period. The symbols denote the variability class

clear that from this point of view the SRVs cannot be a short-period extension of the Miras. Hence, it seems that the pulsation mode does not have a drastic influence on the gas expansion velocity.

#### 4.3. Line intensity ratios

Line intensity ratios can be deduced, since we have observed more than one transition per star for a number of objects. We have used only high-quality spectra and no upper limits. The results for the  $2-1/1-0$ -ratio are on average 4.2 at SEST (15 objects) and 3.0 at IRAM (2 objects). For the  $3-2/2-1$ - and  $4-3/3-2$ -ratios the results are 1.8 (9 objects) and 1.1 (7 objects), respectively, at JCMT. One may conclude from this that up to the  $3-2$  line the intensity increases significantly with increasing  $J$ -levels. However, the exact increase with  $J$ -level is uncertain, since we find an intensity ratio in the  $2-1$  line between SEST and JCMT of 0.7 (4 objects), possibly indicating a discrepancy in the absolute calibration of this line at either or both telescopes. We find that there is a considerable spread in the intensity ratios (within each group), by more than a factor of three. Parts of this is certainly due to uncertainties in the calibrations (incl. pointing problems, etc.), but the different natures of the sources probably also add significantly to this.

For optically thin emission with equal beam filling one would expect values of 4, 2.3, and 1.8 for the  $2-1/1-0$ ,  $3-2/2-1$ , and  $4-3/3-1$  line intensity ratios. Thus, our results indicate optically thin emission for the lower J-lines, whereas the higher ones start to saturate. It appears therefore that we observe a very different behaviour than in the case of Mira variables with optically thick envelopes, where a ratio of 2 is typical for the  $2-1/1-0$ -ratio (Groenewegen et al. 1995). Groenewegen et al. also found large ratios for their sample of short period ( $P < 400^d$ ), O-rich Miras. They argued that the CO excitation in thin shells is different, and that possibly radiative excitation could be more important than the one by collisions.

### 5. CO line and IR flux relations

CO radio line emission and far-infrared dust emission are both good probes of the stellar mass-loss on the AGB. The gas and the dust are also connected to each other in the “dust-driven wind”-scenario (Sedlmayr & Dominik 1995). Therefore, an observational test of the correlation of the two emissions can be useful. In Olofsson et al. (1993) integrated CO line intensities, as we present in this paper, were plotted against the IRAS  $60\mu\text{m}$  flux densities. The latter is known to provide a reasonable measure of the dust mass loss rate (Jura 1987). Since we have data from different telescopes and up to four transitions we selected only data from the most frequent observatory/transition combinations for a similar comparison. As argued in Olofsson et al. (1993), as a first approximation, intensities measured at different telescopes should scale in proportion to the beam-areas. In such a way CO (1-0) data from SEST where scaled to the OSO scale by multiplying them with 1.8 (the observational results of Olofsson et al. 1993, suggest a value of 1.5 for visually bright C-stars). For the other transitions only data from a single telescope were used (2-1 from SEST, and 3-2 from JCMT). Plots of  $\log I$  versus  $\log S_{60}$  for the three lines show positive correlations, but with some substantial scatter. The slopes of linear fits are very similar for the three transitions,  $\sim 0.65$ , but considerably lower than the results for the C-stars where the CO line flux varies essentially linearly with the far-infrared flux (slope  $\sim 1.0$ , Olofsson et al. 1993). In order to study this in more detail we have made a first order correction for the distance using K-magnitudes from the literature (mainly SR\_IIa, SR\_IIb, Lb\_I). The resulting diagrams are shown in Fig. 8.

There is very likely a positive correlation in the expected way (e.g., the open circles in the CO(3-2) plot are approximately fitted with a line of slope 1), but the scatter is large in all diagrams. Parts of the scatter in  $I$  can be attributed to calibration uncertainties, but these are expected to be significantly less than 50% for the large majority of the stars. Parts of the scatter in  $S_{60}$  could be a stellar contribution to the  $60\mu\text{m}$  flux density. We have

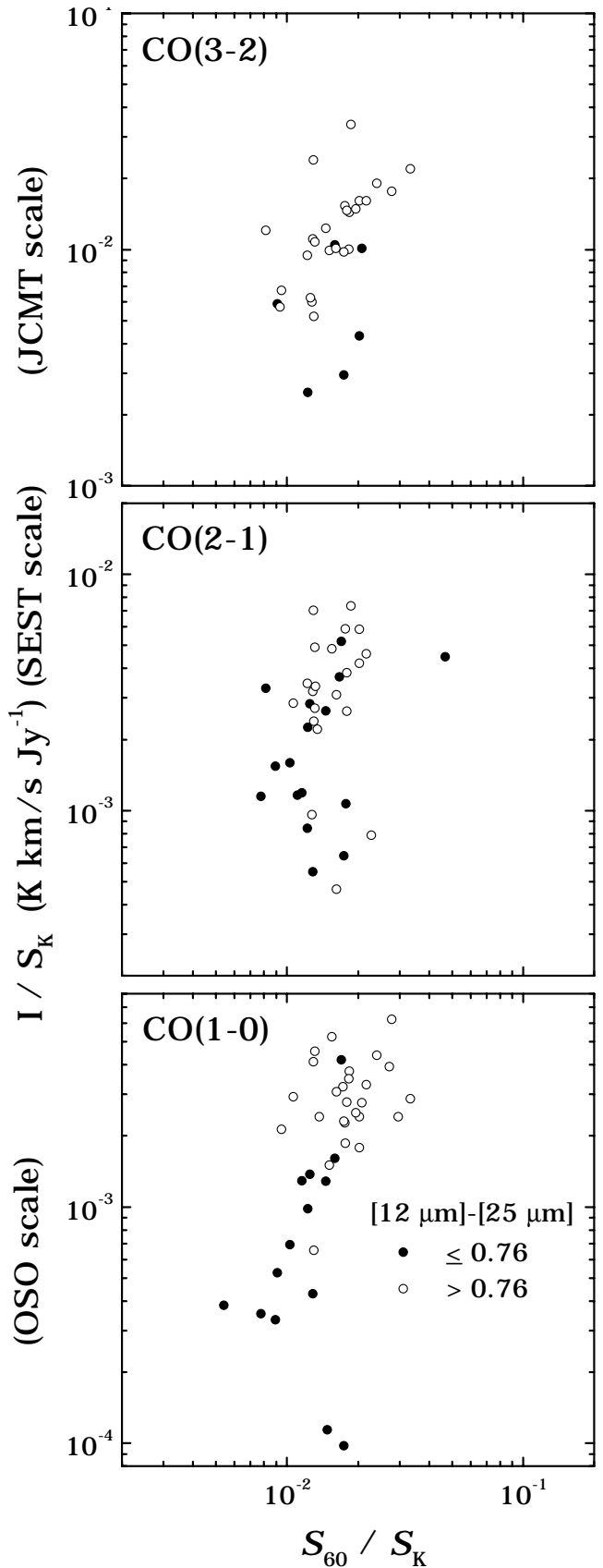


Fig. 8. Plots of distance corrected integrated CO line intensities versus  $60\mu\text{m}$  flux densities

estimated this by fitting combinations of two blackbodies to the spectral energy distributions (see SR\_III). It turns out that the stellar contribution is typically only 10% with a relatively small scatter around this value, and consequently this can only lead to minor shifts in the figures (preferentially shifting the low  $S_{60}/S_K$  objects to the right). The crude distance correction will also lead to a scatter, but it will affect  $I/S_K$  and  $S_{60}/S_K$  in the same way. However, none of these effects can explain the fact that the scatter is substantially larger in  $I/S_K$  than in  $S_{60}/S_K$ . A more detailed analysis of both the CO and the dust emission is required to understand this scatter in detail, but we suggest here that it points to a difference in the mass loss properties of these stars.

We note first that in a given  $S_{60}/K$ -interval the bluer objects (in  $[12 \mu\text{m}] - [25 \mu\text{m}]$ ) lie significantly lower in  $I/S_K$ . We find also that objects with very low  $I/S_K$ -values also have low gas expansion velocities ( $\lesssim 6 \text{ km s}^{-1}$ ). The extreme case is that of L<sup>2</sup> Pup with an expansion velocity of about  $2.5 \text{ km s}^{-1}$ , one of the smallest ever measured for an AGB-star. Some indication of an IR-colour dependence of the gas and dust mass-loss relation is found in Nyman et al. (1992). They found a difference in slope (of linear fits) in  $\log I$  versus  $\log S_{60}$ -diagrammes between objects in regions II and IIIa of the IRAS two-colour diagram (although there are relatively few objects in region II, and both groups may contain C-stars).

We tentatively conclude from this that it is the intergrated CO intensity that is anomalously low for the blue, low  $v_e$  objects (as judged from the IRAS two-colour diagramme the  $60 \mu\text{m}$  flux densities are normal). This could be due to a higher, in a relative sense, dust content in these objects suggesting that dust plays less of a rôle for the gas mass-loss of optically bright, O-rich IRVs and SRVs than it does for higher mass-loss rate O-rich objects and C-stars. Possibly, shock waves or radiation pressure on molecules dominate here (e.g., Höfner et al. 1998). Alternatively, these envelopes are so thin that photodissociation of CO makes CO radio line emission a less reliable mass loss estimator. We cannot exclude that also temporal mass loss rate variations have an effect on this ratio since the CO line and the dust continuum emission do not probe the same regions (epochs).

Recently, Josselin et al. (1996, 1998), argued that the ratio  $S_{60}/T_{\text{mb}}(1-0)$  can be used to discriminate between AGB-stars and supergiants. For the former the ratio falls in the range 20 – 220, while the latter only show ratios  $\gtrsim 200$  (using the IRAM intensity scale for the CO data). In Fig. 9 we present the distribution of this ratio for our sample (OSO scale for the CO data; OSO and SEST data were combined in the way described above). In order to convert to the IRAM scale used in Josselin et al. our values should be divided by about 2.3 (corresponding to the beam area ratios of the OSO 20 m and the IRAM 30 m telescopes; the observed intensity ratio for visually bright C-stars is 1.9, Olofsson et al. 1993), or equivalently, on

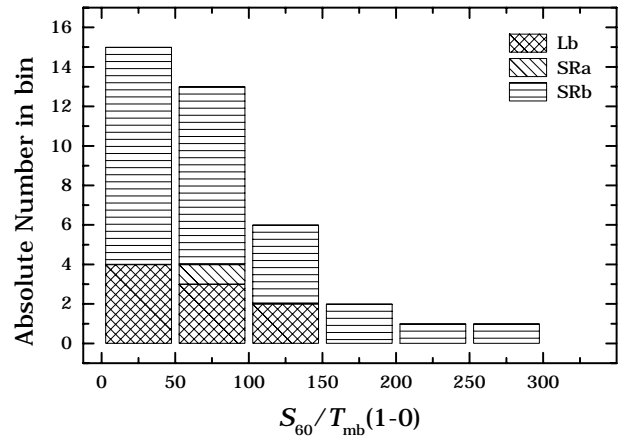


Fig. 9. Distribution of  $S_{60}/T_{\text{mb}}(1-0)$  values (OSO scale)

the OSO scale the range for the AGB-stars is 40 – 500, while for supergiants we have  $\gtrsim 450$ . We find that all our (bona fide) AGB stars fall well below the ratios expected for supergiants. We find also that as many as  $\sim 40\%$  of our stars fall below a ratio of 50, i.e. in a range where Josselin et al. found no stars at all. This is probably due to the fact that our observed sample differs significantly from that of Josselin et al., which is dominated by higher mass loss rate stars as judged from their considerably redder IRAS-colours. In fact, there is essentially no overlap in the IRAS two-colour diagram between the two samples. The most reasonable explanation for the low ratios found in our sample is the significantly lower gas expansion velocities of our stars, which, for a given mass loss rate, decrease the  $S_{60}/T_{\text{mb}}$ -ratio. Possibly, also a lower, in a relative sense, dust content or a different dust composition could play a rôle here. The latter is also indicated by the fact that quite a number of our low mass loss rate objects show a strong  $13 \mu\text{m}$  feature, but no, or a very weak, silicate dust emission feature both in IRAS and ISO spectra (see Sect. 3.4).

## 6. Outlook

In order to determine reliable mass-loss rates and to test the basic assumptions often used in the analysis of circumstellar emission (e.g., spherical symmetry, constant mass loss rate, etc.) we will perform detailed, non-LTE, radiative transfer calculations and compare them with our multi-transition CO observations. This will lead to much more reliable and consistent mass-loss rates than those presented already in SR\_IV and Lb\_IV for part of the objects of this catalogue. These models will be additionally constrained by observations of higher- $J$  lines of CO as well as other molecules (e.g., thermal SiO lines) in order to determine the physical and chemical characteristics of these relatively warm envelopes. In the case of these low mass-loss rate objects, where the higher frequency of peculiar line profiles suggests a complex envelope structure, spatial

information is of particular importance. The most nearby objects can be mapped in suitable molecular emissions with mm-wave interferometers.

*Acknowledgements.* The authors thank the referee Claudine Kahane for constructive comments on the manuscript. The work of FK was supported by APART (Austrian Programme for Advanced Research and Technology) from the Austrian Academy of Sciences. FK was also supported by the Fonds zur Förderung der wissenschaftlichen Forschung under project number S7308-AST and the Österreichische Nationalbank under the Jubiläumsfonds-project number 6876. HO acknowledges financial support from the Swedish Natural Science Research Council.

The authors are very grateful to Martin Groenewegen for providing us with all the valuable IRAM observations in this catalogue. He also contributed a few SEST spectra. Göran Sandell is thanked for carefully performing the JCMT observations, and Andreas Andersson for carefully performing the August-98 SEST observations. The reduction of the CO spectra was made using the DRP software kindly provided by Michael Olberg, OSO.

The Swedish-ESO Submillimetre Telescope, SEST, is operated jointly by ESO and the Swedish National Facility for Radio Astronomy, Onsala Space Observatory at Chalmers University of Technology. The James Clerk Maxwell Telescope is operated by The Joint Astronomy Centre on behalf of the Particle Physics and Astronomy Research Council of the United Kingdom, the Netherlands Organisation for Scientific Research, and the National Research Council of Canada. This research has made use of the SIMBAD database.

## References

- Begeman B., Dorschner J., Henning Th., et al., 1997, *ApJ* 476, 199
- Biegging J.H., Knee L.B.G., Latter W.B., Olofsson H., 1998, *A&A* 339, 811
- Biegging J.H., Latter W.B., 1994, *ApJ* 422, 765
- Bujarrabal V., Alcolea J., Planesas P., 1992, *A&A* 257, 701
- Groenewegen M.A.T., Baas F., Blommaert J., Josselin E., Tilanus R.P.J., 1995, in: "Science with large millimetre arrays", Dec. 1995, Garching, Shaver P. (ed.). Springer Verlag, p. 286
- Groenewegen M.A.T., Baas F., de Jong T., Loup C., 1996, *A&A* 306, 241
- Groenewegen M.A.T., de Jong T., 1998, *A&A* 337, 797
- Höfner S., Jørgensen U.G., Loidl R., Aringer B., 1998, *A&A* 340, 497
- Hu J.Y., te Lintel Hekkert P., Slijkhuis F., Baas F., Sahai R., Wood P.R., 1994, *A&AS* 103, 301
- Josselin E., Loup C., Omont A., Barnbaum C., Nyman L.-A., 1996, *A&A* 315, L23
- Josselin E., Loup C., Omont A., Barnbaum C., Nyman L.A., Sevre F., 1998, *A&AS* 129, 45
- Jura M., 1987, *ApJ* 313, 743
- Jura M., Balm S.P., Kahane C., 1995, *ApJ* 453, 721
- Jura M., Kleinmann S.G., 1992, *ApJS* 79, 105
- Kahane C., Jura M., 1994, *A&A* 290, 183 (K94)
- Kahane C., Jura M., 1996, *A&A* 310, 952
- Kastner J.H., Forveille T., Zuckerman B., Omont A., 1993, *A&A* 275, 163
- Kerschbaum F., Hron J., 1992, *A&A* 263, 97 (SR\_I)
- Kerschbaum F., Hron J., 1994, *A&AS* 106, 397 (SR\_IIa)
- Kerschbaum F., 1995, *A&AS* 113, 441 (SR\_IIb)
- Kerschbaum F., Hron J., 1996, *A&A* 308, 489 (SR\_III)
- Kerschbaum F., Habison P., Hron J., 1996a, Proc.: The Carbon Star Phenomenon, I.A.U. Symposium 177. Kluwer Academic Publishers, Dordrecht (in press)
- Kerschbaum F., Lazaro C., Habison P., 1996b, *A&AS* 118, 397 (Lb\_I)
- Kerschbaum F., Olofsson H., Hron J., 1996c, *A&A* 311, 273 (SR\_IV)
- Kerschbaum F., Olofsson H., Hron J., 1997, in Proc. of of JD24, 23rd GA of the IAU, 17.-30.8.1997, Kyoto, Japan, Sasselov D.D., Takeuti M. (eds.). Universal Academy Press, Inc., Tokyo, Japan, p. 177
- Kerschbaum F., Olofsson H., 1998, *A&A* 336, 654 (Lb\_IV)
- Knapp G.R., Morris M., 1985, *ApJ* 292, 640
- Knapp G.R., Sutin B.M., Phillips T.G., Ellison B.N., Keene J.B., Leighton R.B., Masson C.R., Steiger W., Veidt B., Young K., 1989, *ApJ* 336, 822
- Kahane C., Barnbaum C., Uchida K., Balm S.P., Jura M., 1998, *ApJ* 500, 466
- Knapp G. R., Young K., Lee E., Jorissen A., 1998, *ApJS* 117, 209
- Leahy D.A., Kwok S., Arquilla R.A., 1987, *ApJ* 320, 825
- Lebzelter T., Kerschbaum F., Hron J., 1995, *A&A* 298, 159
- Likkel L., Forveille T., Omont A., Morris M., 1991, *A&A* 246, 153
- Loup C., Forveille T., Omont A., Nyman L.A., 1990, *A&A* 227, 29L
- Loup C., Forveille T., Omont A., Paul J.F., 1993, *A&AS* 99, 291 (L93)
- Margulis M., van Blerkom D.J., Snell R.L., Kleinmann S.G., 1990, *ApJ* 361, 673
- Nguyen-Quang-Rieu, Epchtein N., Truong-Bach, Cohen M., 1987, *A&A* 180, 117
- Nyman L.-Å., Booth R.S., Carlström U., et al., 1992, *A&AS* 93, 121
- Olofsson H., Eriksson K., Gustafsson B., Carlström U., 1993, *ApJS* 87, 267
- Sedlmayr E., Dominik C., 1995, *Sp. Sc. Rev.* 73, 211
- Sahai R., Liechti S., 1995, *A&A* 293, 193
- van der Veen W.E.C.J., Habing H., 1988, *A&A* 194, 125
- van der Veen W.E.C.J., Trams N.R., Waters L.B.F.M., 1993, *A&A* 269, 231
- Volk K., Kwok S., Woodsworth A.W., 1993, *ApJ* 402, 292
- Wood P.R., 1990, Proc.: From Miras to Planetary Nebulae, Mennessier M.O., Omont A. (eds.). Éditions Frontières, Gif-sur-Yvette, p. 67
- Young K., 1995, *ApJ* 445, 872 (Y95)
- Zuckerman B., Dyck H.M., 1986, *ApJ* 304, 394
- Zuckerman B., Dyck H.M., Claussen M.J., 1986, *ApJ* 304, 401

## Appendix A: Catalogues and spectra

**Table A1.** Basic data of the observed O-rich AGB variables (Part 1)

GCVS4	IRAS	Type	RA (2000.0)	DE	Source	Period (d)
UY Cet	00245-0652	SRb	00 27 06.37	-06 36 16.6	Sim	440
VY Cas	00484+6238	SRb	00 51 26.12	62 55 14.8	HIC	100
CE And	01265+4624	Lb	01 29 33.24	46 39 33.5	GSC	
SV Psc	01438+1850	SRb	01 46 35.33	19 05 04.7	Sim	102
UX And	02302+4525	SRb	02 33 28.64	45 39 16.4	Sim	400
W Hor	02427-5430	SRb	02 44 14.70	-54 18 04.0	ISO	137
T Ari	02455+1718	SRa	02 48 19.74	17 30 34.5	HIC	317
SS Cep	03415+8010	SRb	03 49 29.84	80 19 21.0	HIC	90
SU Eri	03489-0131	SRb	03 51 27.03	-01 22 16.2	TYC	112
U Men	04140-8158	SRa	04 09 35.71	-81 51 18.0	HIC	407
IR Per	04166+4056	SRa	04 20 03.09	41 03 50.6	Sim	175
RV Cam	04265+5718	SRb	04 30 41.78	57 24 42.2	HIC	101
R Dor	04361-6210	SRb	04 36 45.67	-62 04 38.2	HIC	338
RX Lep	05090-1154	SRb	05 11 22.87	-11 50 57.1	HIC	60
V1057 Ori	05152+1321	SRb	05 18 04.12	13 25 03.8	HIC	67
EX Ori	05220-0611	Lb	05 24 28.75	-06 08 48.9	Sim	
DV Tau	05281+1831	Lb	05 31 06.31	18 33 38.9	Sim	
GP Tau	05354+2458	SRb	05 38 32.63	25 00 06.9	TYC	90
RW Lep	05365-1404	SRa	05 38 52.60	-14 02 26.2	GSC	150
AB Tau	05378+2804	SRa	05 41 02.45	28 06 23.3	HIC	142
TW Aur	05534+4530	SRb	05 57 06.75	45 30 34.2	TYC	150
V352 Ori	05592-0221	Lb	06 01 46.81	-02 21 13.0	Sim	
S Lep	06036-2411	SRb	06 05 45.60	-24 11 43.9	HIC	89
VW Aur	06139+3313	SRb	06 17 14.35	33 12 23.0	TYC	220
AQ Gem	06261+1637	Lb	06 26 06.36	16 37 54.4	GSC	
DW Gem	06278+2729	Lb	06 30 59.74	27 27 07.8	Sim	
GL Mon	06333-0520	SRb	06 33 18.89	-05 20 07.1	GSC	104
X CMa	06546-2353	SRb	06 56 45.94	-23 57 55.4	TYC	107
L <sup>2</sup> Pup	07120-4433	SRb	07 13 32.31	-44 38 22.7	HIC	141
HU Pup	07536-2830	SRa	07 55 40.18	-28 38 55.5	Sim	238
FZ Hya	08189+0507	Lb	08 21 33.24	04 57 30.5	Sim	
OT Pup	08200-2528	Lb	08 22 11.10	-25 37 55.0	Sim	
FK Hya	08220-0821	Lb	08 24 27.89	-08 31 12.7	HIC	
AK Hya	08375-1707	SRb	08 39 53.60	-17 18 11.0	HIC	75
EP Vel	08400-4755	SRa	08 41 41	-48 06 48	GCVS4	240
EY Hya	08437+0149	SRa	08 46 21.25	01 37 56.1	HIC	183
CW Cnc	09057+1325	Lb	09 08 26.58	13 13 13.7	HIC	
SY Vel	09105-4334	SRb	09 12 25.74	-43 46 38.8	TYC	63
SU Vel	09480-4147	SRb	09 50 02.54	-42 01 16.5	GSC	150
RR Car	09564-5837	SRb	09 58 04.83	-58 51 40.5	TYC	
UV Car	10226-6039	Lb	10 22 38.45	-60 39 16.3	GSC	
CT UMa	10305+7001	Lb	10 34 16.70	69 45 53.0	Sim	
BI Car	10416-6313	Lb	10 41 41.26	-63 13 17.4	GSC	
R Crt	10580-1803	SRb	11 00 33.98	-18 19 28.5	HIC	160
CS Dra	11125+7524	Lb	11 15 56.20	75 08 32.0	Sim	
AZ UMa	11445+4344	Lb	11 47 13.80	43 28 16.4	HIC	
RW Vir	12046-0629	Lb	12 07 14.96	-06 45 56.5	HIC	
BK Vir	12277+0441	SRb	12 30 20.98	04 24 59.1	HIC	150
Y UMa	12380+5607	SRb	12 40 21.27	55 50 47.5	HIC	168
RT Vir	13001+0527	SRb	13 02 38.00	05 11 08.2	HIC	155
SW Vir	13114-0232	SRb	13 14 04.34	-02 48 24.5	HIC	150
V CVn	13172+4547	SRa	13 19 27.77	45 31 38.0	HIC	192
V744 Cen	13368-4941	SRb	13 39 59.77	-49 57 00.2	HIC	90
W Hya	13462-2807	SRa	13 49 02.09	-28 22 03.2	HIC	361
V806 Cen	13465-3412	SRb	13 49 26.72	-34 27 02.6	HIC	12

**Table A2.** Basic data of the observed O-rich AGB variables (Part 2)

GCVS4	IRAS	Type	RA	DE	Source	Period
			(2000.0)			(d)
$\theta$ Aps	14003-7633	SRb	14 05 19.83	-76 47 48.3	HIC	119
RX Boo	14219+2555	SRb	14 24 11.62	25 42 13.3	HIC	340
RV Boo	14371+3245	SRb	14 39 15.86	32 32 22.3	HIC	137
$\tau^4$ Ser	15341+1515	SRb	15 36 28.19	15 06 04.4	HIC	100
X Her	16011+4722	SRb	16 02 39.15	47 14 25.1	HIC	95
$g$ Her	16269+4159	SRb	16 28 38.55	41 52 53.7	HIC	89
S Dra	16418+5459	SRb	16 42 55.95	54 54 12.7	HIC	136
AH Dra	16473+5753	SRb	16 48 16.53	57 48 49.0	HIC	158
V438 Oph	17123+1107	SRb	17 14 39.78	11 04 10.5	HIC	170
TY Dra	17361+5746	Lb	17 37 00.01	57 44 25.8	Sim	
V774 Sgr	17513-2313	Lb	17 54 26.15	-23 14 09.4	HIC	
TU Lyr	18186+3143	Lb	18 20 30.20	31 45 21.4	Sim	
CZ Ser	18347-0241	Lb	18 37 20.98	-02 39 14.0	GSC	
V3879 Sgr	18399-1920	SRb	18 42 55.11	-19 17 03.2	HIC	50
UX Sgr	18520-1635	SRb	18 54 54.48	-16 31 31.3	TYC	100
R Lyr	18537+4352	SRb	18 55 20.11	43 56 45.9	HIC	46
SU Sgr	19007-2247	SRb	19 03 43.81	-22 42 42.6	HIC	60
YZ Lyr	19014+2904	Lb	19 03 25.44	29 08 50.6	GSC	
V347 Aql	19055+0613	Lb	19 08 01.11	06 18 27.6	GSC	
SZ Dra	19098+6601	Lb	19 10 02.30	66 06 09.9	HIC	
V Tel	19143-5032	SRb	19 18 14.60	-50 26 48.2	TYC	125
T Sge	19194+1734	SRb	19 21 42.05	17 40 00.1	HIC	166
S Pav	19510-5919	SRa	19 55 13.90	-59 11 43.8	HIC	381
NU Pav	19575-5930	SRb	20 01 44.72	-59 22 33.6	HIC	60
V1943 Sgr	20038-2722	Lb	20 06 55.24	-27 13 29.9	HIC	
X Pav	20075-6005	SRb	20 10 45.59	-59 56 12.0	Sim	199
V584 Aql	20079-0146	Lb	20 10 29.72	-01 37 40.3	Sim	
Y Tel	20165-5051	Lb	20 20 14.30	-50 42 12.0	Sim	
UU Dra	20248+7505	SRb	20 24 03.50	75 15 13.6	HIC	120
T Mic	20248-2825	SRb	20 27 55.22	-28 15 39.9	HIC	347
TZ Aql	20276-0455	Lb	20 30 18.50	-04 45 16.7	HIC	
V397 Cyg	20302+3517	Lb	20 32 12.23	35 27 08.3	Sim	
U Del	20431+1754	SRb	20 45 28.26	18 05 24.5	HIC	110
FI Vul	20466+2248	Lb	20 48 51.18	22 59 38.9	HIC	
RZ Cyg	20502+4709	SRa	20 51 54	47 21 24	GCVS4	276
IN Vul	20511+2523	Lb	20 53 21.96	25 35 00.1	GSC	
SX Pav	21243-6943	SRb	21 28 44.86	-69 30 19.4	HIC	50
W Cyg	21341+4508	SRb	21 36 02.49	45 22 28.8	HIC	131
RU Cyg	21389+5405	SRa	21 40 39.07	54 19 29.3	HIC	233
EP Aqr	21439-0226	SRb	21 46 31.86	-02 12 45.7	HIC	55
TW Peg	22017+2806	SRb	22 03 59.54	28 20 54.0	HIC	929
SV Peg	22035+3506	SRb	22 05 42.07	35 20 53.8	HIC	145
$\epsilon$ Oct	22145-8041	SRb	22 20 01.50	-80 26 23.1	HIC	55
AB Aqr	22359-1417	Lb	22 38 34.51	-14 02 15.1	Sim	
V PsA	22525-2952	SRb	22 55 19.66	-29 36 44.2	TYC	148
BC And	22586+4614	Lb	23 00 53.05	46 30 38.2	Sim	
V352 Cep	22594+6117	Lb	23 01 27.20	61 33 48.0	Sim	
AS Cep	23000+5932	Lb	23 02 05.20	59 49 06.0	Sim	
CF And	23013+3735	Lb	23 03 43.71	37 51 13.7	Sim	
Y Scl	23063-3024	SRb	23 09 05.55	-30 08 02.2	HIC	
SV Aqr	23201-1105	Lb	23 22 45.00	-10 49 02.0	Sim	
V530 Cas	23284+5958	Lb	23 30 44.10	60 15 21.0	Sim	
SV Cas	23365+5159	SRa	23 39 01.37	52 15 45.1	HIC	265
RS And	23528+4821	SRa	23 55 21.73	48 38 17.8	TYC	136

**Table A3.** Observational results of O-rich Lb variables (Part 1)

GCVS4	IRAS	Code	S	$I$ (Kkm s <sup>-1</sup> )	$T_{\text{mb}}$ (K)	$I_{\text{r/b}}$	$v_{\text{hel}}$ (km s <sup>-1</sup> )	$v_{\text{LSR}}$ (km s <sup>-1</sup> )	$v_{\text{e}}$ (km s <sup>-1</sup> )	Q	C
CE And	01265+4624	O10	N	0.72						5	
		J32	D	1.71:	0.10		-17.5:	-14.6	11.5:	4	
EX Ori	05220-0611	S21	D	0.52	0.07		-12.6	-30.6	5.2	2	
		J32	D	2.30	0.18		-12.7:	-30.8	8.0:	4	
DV Tau	05281+1831	S10	N	0.34						5	
		S21	N	0.46						5	
V352 Ori	05592-0221	S21	Di	0.38	0.04		38.8:	21.1	8.4:	2	
AQ Gem	06261+1637	S10	N	0.54						5	
		S21	N	0.39						5	
DW Gem	06278+2729	O10	N	0.31						5	
FZ Hya	08189+0507	O10	N	0.71						5	
		S21	D	1.67	0.12	1.01	0.5	-12.9	10.4	2	
OT Pup	08200-2528	J32	D	4.56	0.35	1.15	0.1	-13.3	8.3	1	
		S21	D	1.48	0.10	1.23	48.1	30.9	10.6	1	
FK Hya	08220-0821	J32	D	6.82	0.39	0.95	48.0	30.8	13.6	2	
		S21	D	0.37	0.02		55.5	40.0	12.6	3	
CW Cnc	09057+1325	J32	N	0.63						5	
		O10	D	2.51	0.16	1.21	26.7	17.3	8.4	2	
UV Car	10226-6039	S21	D	4.29	0.25	1.00	25.3	15.9	9.9	1	
		J32	D	14.61	1.01	1.10	25.0	15.6	10.5	1	
CT UMa	10305+7001	S10	Ni							5	
		S21	Ni							5	
BI Car	10416-6313	O10	N	0.65						5	
CS Dra	11125+7524	S10	N	0.30						5	
		S21	D	0.34	0.11		-1.6	-13.2	2.6	2	
AZ UMa	11445+4344	O10	D	1.34	0.06		-58.5	-49.8	11.6	3	
		J32	D	3.84	0.29		-59.0	-50.3	8.8:	3	
RW Vir	12046-0629	O10	D	0.58	0.08		-49.7	-43.7	4.0	3	
		J32	D	4.42	0.62	1.19	-49.5	-43.5	5.5	1	
TY Dra	17361+5746	S21	D	1.88	0.17	1.35	21.8	20.9	8.0	1	
		J32	D	6.88	0.56	1.07	22.3	21.3	7.2	1	
V774 Sgr	17513-2313	O10	D	1.08	0.06		-34.9:	-17.3	9.7:	2	
		I21	D	11.50	0.80		-34.5	-16.9	11.2	1	
TU Lyr	18186+3143	S10	Ni							5	
		S21	Ni							5	
CZ Ser	18347-0241	O10	N	0.73						5	
		I10	D	1.90	0.12		-10.1	9.9	8.4	2	
YZ Lyr	19014+2904	I21	D	5.70	0.45		-10.2	9.8	8.0	2	
		I10	Di	3.85:	0.21		-31.1:	-14.5	9.2:	3	
V347 Aql	19055+0613	I21	Di	11.43	0.71		-31.5	-14.8	9.8	2	
		O10	N	0.80						5	
SZ Dra	19098+6601	S10	Ni							5	
		S21	Ni							5	
V1943 Sgr	20038-2722	O10	D	0.77	0.05		-42.0:	-26.1	9.6:	3	
		S10	D	1.25	0.12		-22.5	-13.9	7.6	1	
V584 Aql	20079-0146	S21	D	5.17	0.53	0.91	-23.2	-14.6	6.5	3	
		J32	D	5.70:	1.40	1.01	-23.7	-15.0	6.5	2	
Y Tel	20165-5051	S21	D	0.87	0.12		-13.6	0.9	3.3	2	
TZ Aql	20276-0455	S10	D	0.32	0.04		-45.8	-44.4	6.4	3	
		S21	D	0.54	0.08	0.67	-45.7	-44.3	4.4	2	
V397 Cyg	20302+3517	S10	N	0.74						5	
		S21	D	0.62	0.07	1.04	49.1	62.1	6.2	2	
FI Vul	20466+2248	O10	Ni	1.62						5	
IN Vul	20511+2523	O10	N	1.14						5	
				2.79						5	

**Table A4.** Observational results of O-rich Lb variables (Part 2)

GCVS4	IRAS	Code	S	$I$ (Kkm s <sup>-1</sup> )	$T_{\text{mb}}$ (K)	$I_{\text{r/b}}$	$v_{\text{hel}}$ (km s <sup>-1</sup> )	$v_{\text{LSR}}$ (km s <sup>-1</sup> )	$v_e$ (km s <sup>-1</sup> )	Q	C
AB Aqr	22359-1417	S10	N	0.67						5	
		S21	D	0.85	0.10		29.3	33.1	5.1	2	
BC And	22586+4614	O10	D	0.58	0.08		-12.2:	-1.7	4.5:	3	
V352 Cep	22594+6117	O10	Ni							5	
AS Cep	23000+5932	O10	N	1.35						5	
CF And	23013+3735	O10	N	0.44						5	
SV Aqr	23201-1105	S10	D	0.74	0.06		6.4:	7.6	10.5:	3	
		S21	D	1.23	0.09		4.7	5.9	7.9	2	
V530 Cas	23284+5958	O10	Ni							5	

**Table A5.** Observational results of O-rich SRa variables

GCVS4	IRAS	Code	S	$I$ (Kkm s <sup>-1</sup> )	$T_{\text{mb}}$ (K)	$I_{\text{r/b}}$	$v_{\text{hel}}$ (km s <sup>-1</sup> )	$v_{\text{LSR}}$ (km s <sup>-1</sup> )	$v_e$ (km s <sup>-1</sup> )	Q	C
T Ari	02455+1718	S10	N	0.21						5	
		S21	D	0.65	0.14	1.12	6.4	-1.4	3.2	1	
U Men	04140-8158	S10	N	0.40						5	
		S21	D	2.31	0.18		24.4	12.3	8.5	2	
IR Per	04166+4056	O10	Ni	1.38						5	
RW Lep	05365-1404	S10	N	0.25						5	
		S21	D	0.37	0.05		-38.9	-58.0	5.8:	3	
AB Tau	05378+2804	O10	N	1.35						5	
HU Pup	07536-2830	S10	Ni							5	
EP Vel	08400-4755	S10	Ni							5	
EY Hya	08437+0149	S10	N	0.41						5	
		S21	D	1.96	0.10	0.86	35.2	22.3	14.4	2	
		J32	D	6.81	0.40	1.01	35.7	22.8	11.7	2	
V CVn	13172+4547	O10	N	0.36						5	
W Hya	13462-2807	S10	D	0.83:	0.06		38.7	40.7	7.2	3	
S Pav	19510-5919	S10	N	0.66						5	
		S21	D	2.00	0.12		-19.1	-19.9	9.3	2	
RZ Cyg	20502+4709	O10	Ni							5	
RU Cyg	21389+5405	O10	Ni							5	
SV Cas	23365+5159	O10	N	1.44						5	
RS And	23528+4821	O10	D	0.92	0.15		-2.1	5.4	6.1	2	
		J32	D	5.98	0.77		-0.8	6.7	5.0	3	

**Table A6.** Observational results of O-rich SRb variables (Part 1)

GCVS4	IRAS	Code	S	$I$ (Kkm s <sup>-1</sup> )	$T_{\text{mb}}$ (K)	$I_{\text{r/b}}$	$v_{\text{hel}}$ (km s <sup>-1</sup> )	$v_{\text{LSR}}$ (km s <sup>-1</sup> )	$v_e$ (km s <sup>-1</sup> )	Q	C
UY Cet	00245-0652	S10	D	0.76	0.07		8.4	5.5	8.0	2	
		S21	D	3.31	0.30	1.23	7.5	4.6	7.3	1	
		J32	D	9.07	1.02	1.05	7.5	4.6	7.0	1	
VY Cas	00484+6238	O10	Ni	1.50						5	
SV Psc	01438+1850	S10	D	0.69	0.05		10.7	6.9	11.9	3	b+n
		O10	D	0.69	0.17		9.8:	6.0	8.1:	3	b+n
		S21	D	2.18	0.27		9.1	5.3	12.7	1	b+n
		S21	D	0.48	0.19		10.2	6.4	2.3	1	n
UX And	02302+4525	S21	D	1.52	0.10		10.4	6.6	10.8	1	b
		O10	D	1.50	0.06		-17.7	-18.4	17.0	3	
		J32	D	6.34	0.32		-19.7	-20.4	12.9	3	
W Hor	02427-5430	S10	N	0.64						5	
		S21	N	1.17						5	
SS Cep	03415+8010	O10	D	2.38	0.12		-48.3	-40.9	11.3	2	
		J32	D	7.50	0.45	1.12	-48.1	-40.7	9.9	2	
SU Eri	03489-0131	S10	N	0.29						5	
		S21	N	0.08						5	
RV Cam	04265+5718	O10	D	0.98:	0.08		-16.2	-16.3	6.7	2	
		J32	D	5.81	0.60	0.93	-15.4	-15.5	6.2	1	
R Dor	04361-6210	S10	D	5.00	0.38		23.5	7.1	6.1	2	
		S21	D	41.6	3.53	0.93	23.2	6.8	7.2	1	
		S32	D	70.4	6.20	1.01	23.8	7.4	6.9	1	
RX Lep	05090-1154	S10	D	0.47	0.05		29.8	11.3	8.2:	3	
		S21	D	2.78	0.45	1.06	28.6	10.0	4.8	1	
V1057 Ori	05152+1321	S10	Ni							5	
GP Tau	05354+2458	S10	Ni							5	
		S21	Ni							5	
TW Aur	05534+4530	O10	N	0.96						5	
S Lep	06036-2411	S10	N	0.92						5	
		S21	N	0.43						5	
VW Aur	06139+3313	O10	N	1.78						5	
GL Mon	06333-0520	S10	N	0.58						5	
		S21	N	0.42						5	
X CMa	06546-2353	S10	N	0.69						5	
		S21	N	0.49						5	
L <sup>2</sup> Pup	07120-4433	S10	D	0.29	0.08		52.1	33.3	2.0	2	
		S21	D	3.44	0.81	0.87	52.2	33.4	3.3	1	
		J21	D	3.60	1.07		51.7	32.9	2.3	2	
AK Hya	08375-1707	J32	D	15.76	3.78	0.78	52.5	33.7	3.0	1	
		S10	D	0.43	0.08		35.0	19.2	4.6	3	
		S21	D	2.79	0.30	1.43	34.1	18.3	6.3	1	
		J21	D	4.32	0.51		35.6	19.8	5.0	2	
SY Vel	09105-4334	J32	D	6.11	0.74	0.86	35.4	19.6	5.8	1	
		S10	Ni							5	
SU Vel	09480-4147	S21	Ni							5	
		S10	Di	0.82	0.09		21.3	7.5	5.7	3	
RR Car	09564-5837	S21	Di	3.49	0.36	1.31	20.9	7.1	6.6	1	
		J21	D	6.85	0.64	1.18	21.4	7.6	6.0	1	
		J32	D	3.59	0.33	1.03	21.6	7.8	6.9	2	
		S10	Ni							5	
R Crt	10580-1803	S21	Ni							5	
		S10	D	5.00					10.3	2	
		J21	D	24.05	1.20	1.13	18.8	11.2	11.4	1	
		J32	D	39.20	2.00	1.04	19.1	11.5	11.4	1	
		J43	D	54.12	2.65		18.8	11.2	11.7	2	



**Table A8.** Observational results of O-rich SRb variables (Part 3)

GCVS4	IRAS	Code	S	$I$ (Kkm s <sup>-1</sup> )	$T_{\text{mb}}$ (K)	$I_{\text{r/b}}$	$v_{\text{hel}}$ (km s <sup>-1</sup> )	$v_{\text{LSR}}$ (km s <sup>-1</sup> )	$v_e$ (km s <sup>-1</sup> )	Q	C
NU Pav	19575–5930	S10	N	0.39						5	
		S21	N	0.36						5	
X Pav	20075–6005	S10	N	0.24						5	
		S21	N	0.10						5	
UU Dra	20248+7505	O10	D	2.93	0.19	1.09	–41.9	–28.6	9.5	2	
		J32	D	8.29	0.55	1.00	–40.5	–27.2	9.0	2	
T Mic	20248–2825	S10	D	1.20	0.10		19.1	26.7	8.7:	3	
		S21	D	5.00	0.55	0.98	17.5	25.1	6.1	1	
U Del	20431+1754	O10	D	2.96	0.18	0.84	–22.0	–6.4	8.6	2	
		S21	D	2.87	0.19	1.06	–22.2	–7.8	8.7	1	
SX Pav	21243–6943	S10	N	0.50						5	
W Cyg	21341+4508	O10	D	1.24	0.08		–14.0:	0.4	7.6:	2	
		J32	D	13.89	0.90	0.92	–14.3	0.1	9.0	2	
EP Aqr	21439–0226	S10	D	3.90:	0.22		–42.9	–33.5	10.2	3	b+n
		S10	D	0.72	0.42		–43.1	–33.7	1.5	1	n
		S10	D	4.85	0.29		–43.1	–33.7	10.7	1	b
TW Peg	22017+2806	S10	D	1.84	0.09	0.83	–23.5	–11.1	11.9	2	
		O10	D	1.66	0.10		–24.3	–11.9	9.6	2	
		S21	D	5.01	0.29	1.05	–23.9	–11.5	10.8	1	
		J32	D	17.48	1.02	1.03	–22.9	–10.5	10.2	1	
SV Peg	22035+3506	O10	D	3.54	0.20		–6.7	6.1	10.7	2	
		S21	D	4.97	0.39	1.03	–6.9	5.5	7.4	1	
		J32	D	17.32	1.39	0.98	–6.7	5.7	8.3	1	
ε Oct	22145–8041	S10	N	0.79						5	
V PsA	22525–2952	S10	N	0.63						5	
		S21	D	4.00	0.15	0.88	–10.6	–11.1	14.4	1	
Y Scl	23063–3024	S10	D	0.37	0.04		30.5	29.0	7.3	3	
		S21	D	1.38	0.16	1.17	30.0	28.6	5.9	1	

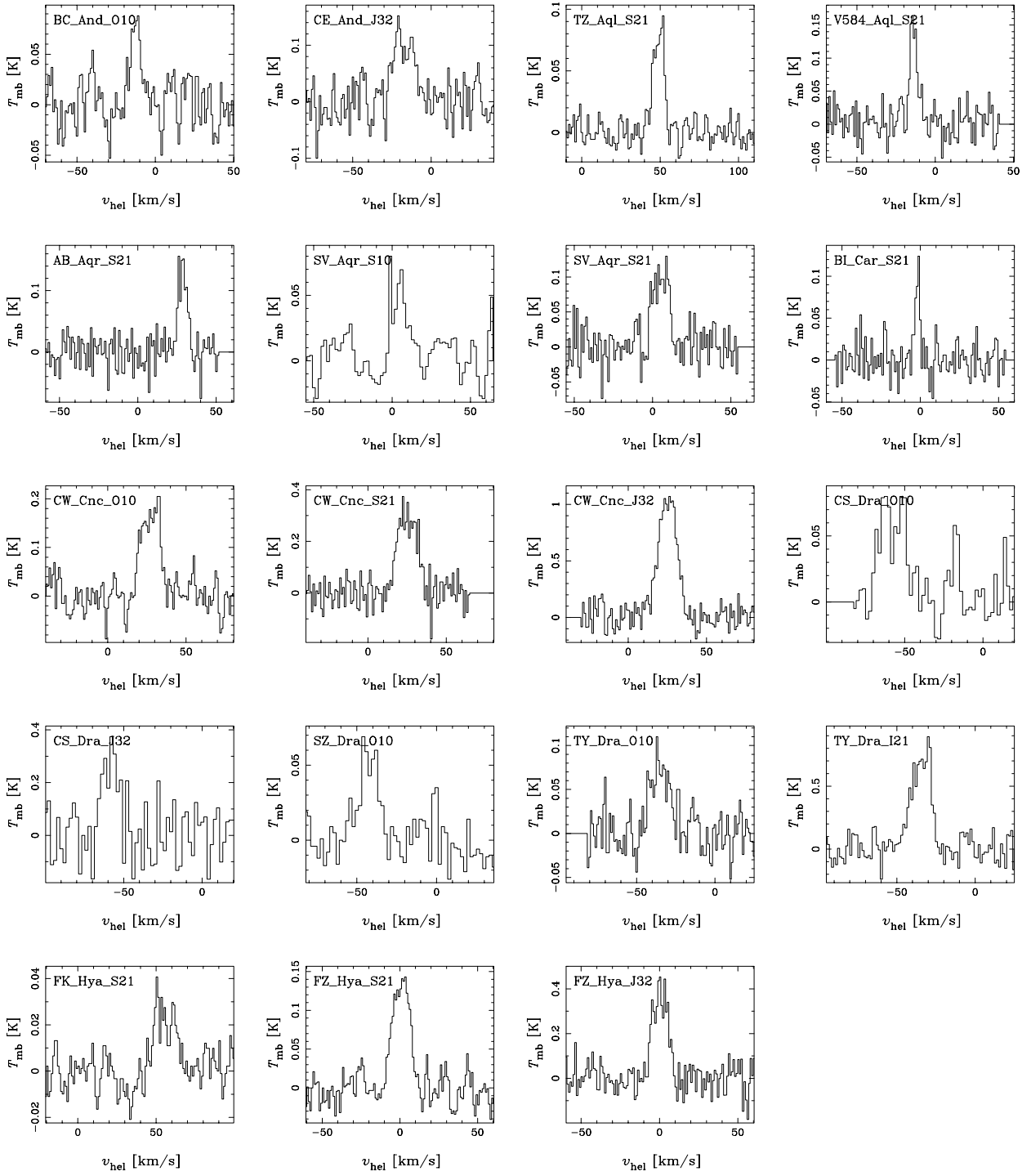


Fig. A1. CO spectra of O-rich Lb variables (Part 1)

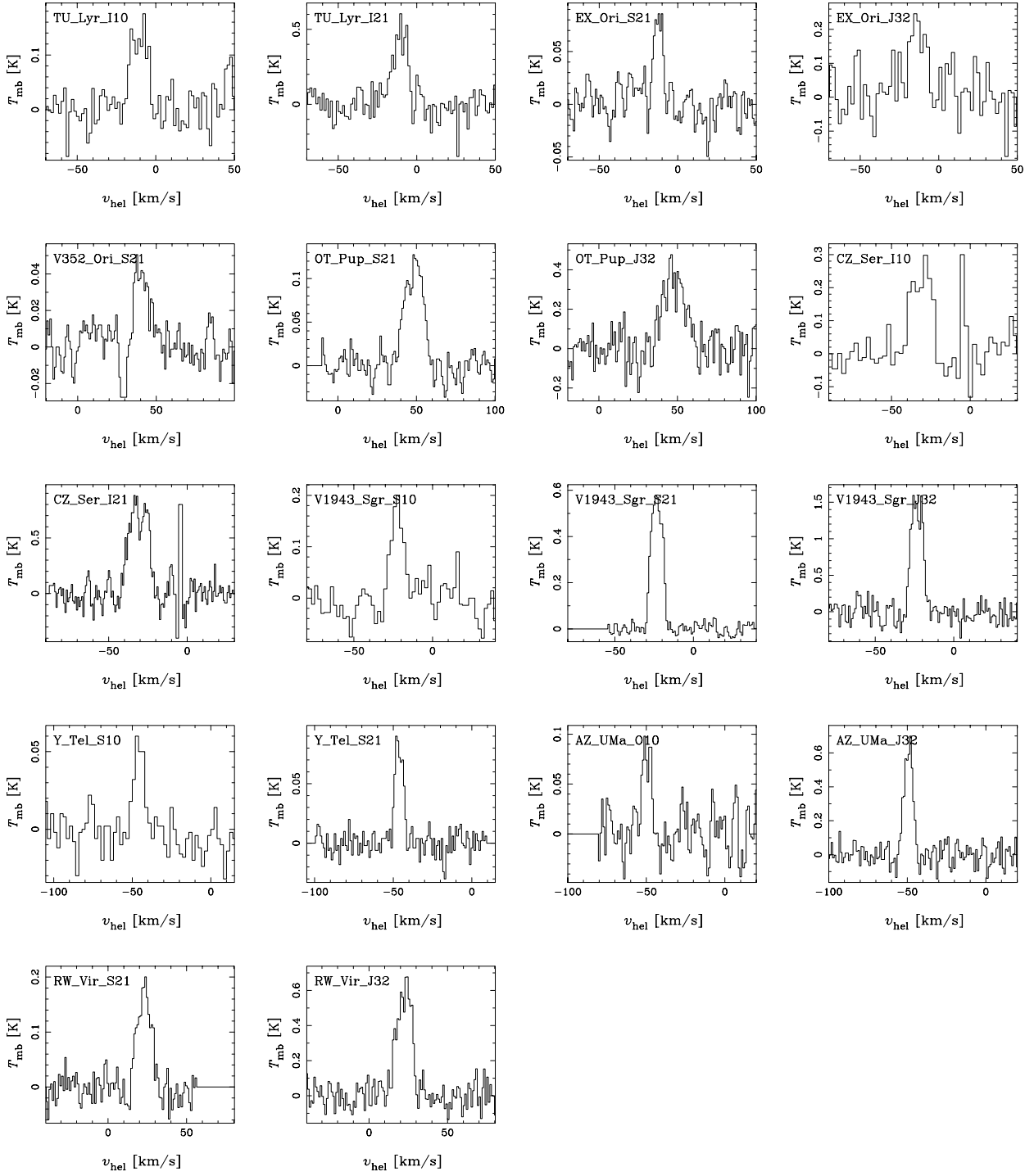


Fig. A2. CO spectra of O-rich Lb variables (Part 2)

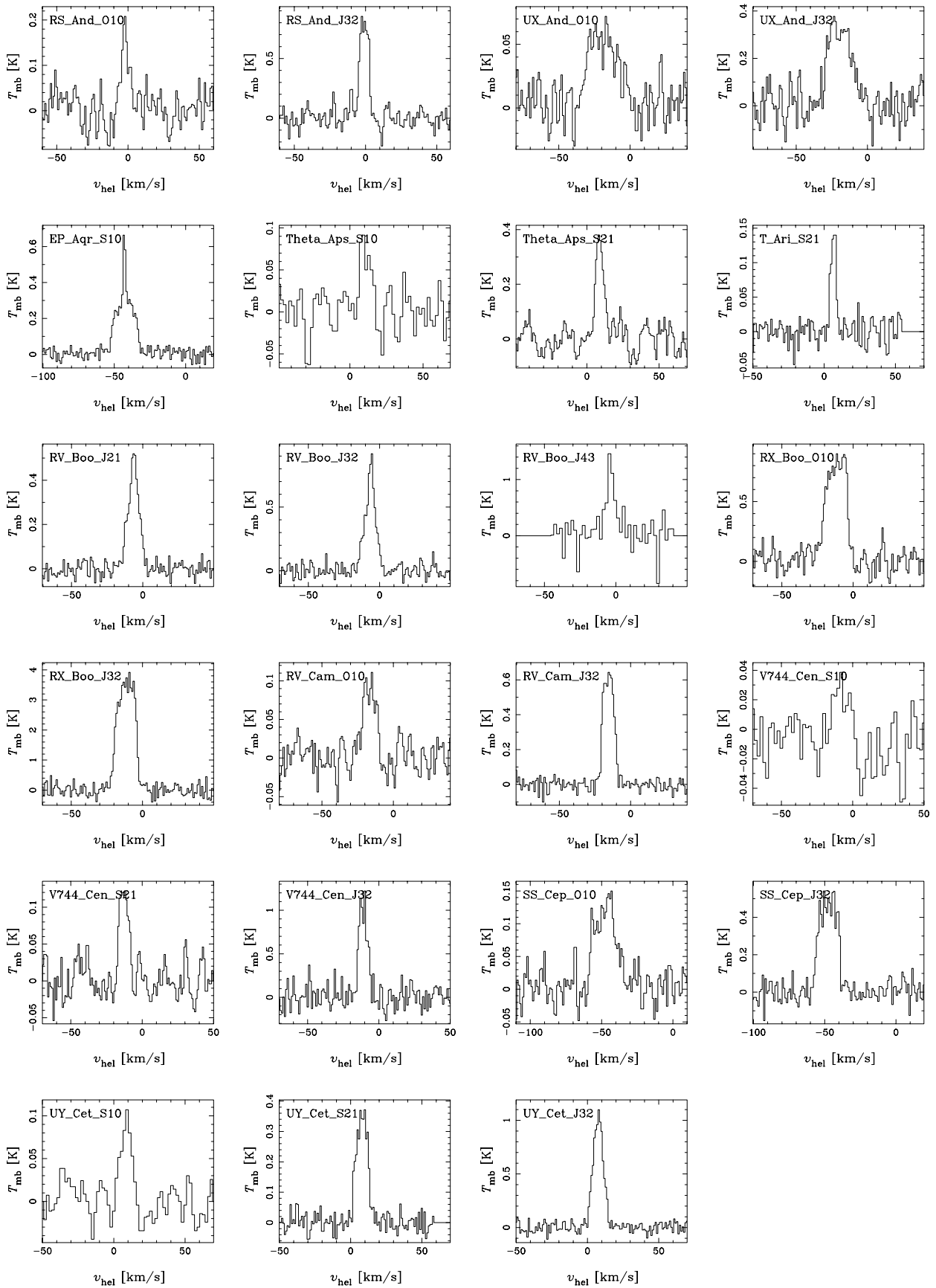


Fig. A3. CO spectra of O-rich SRA and SRb variables (Part 1)

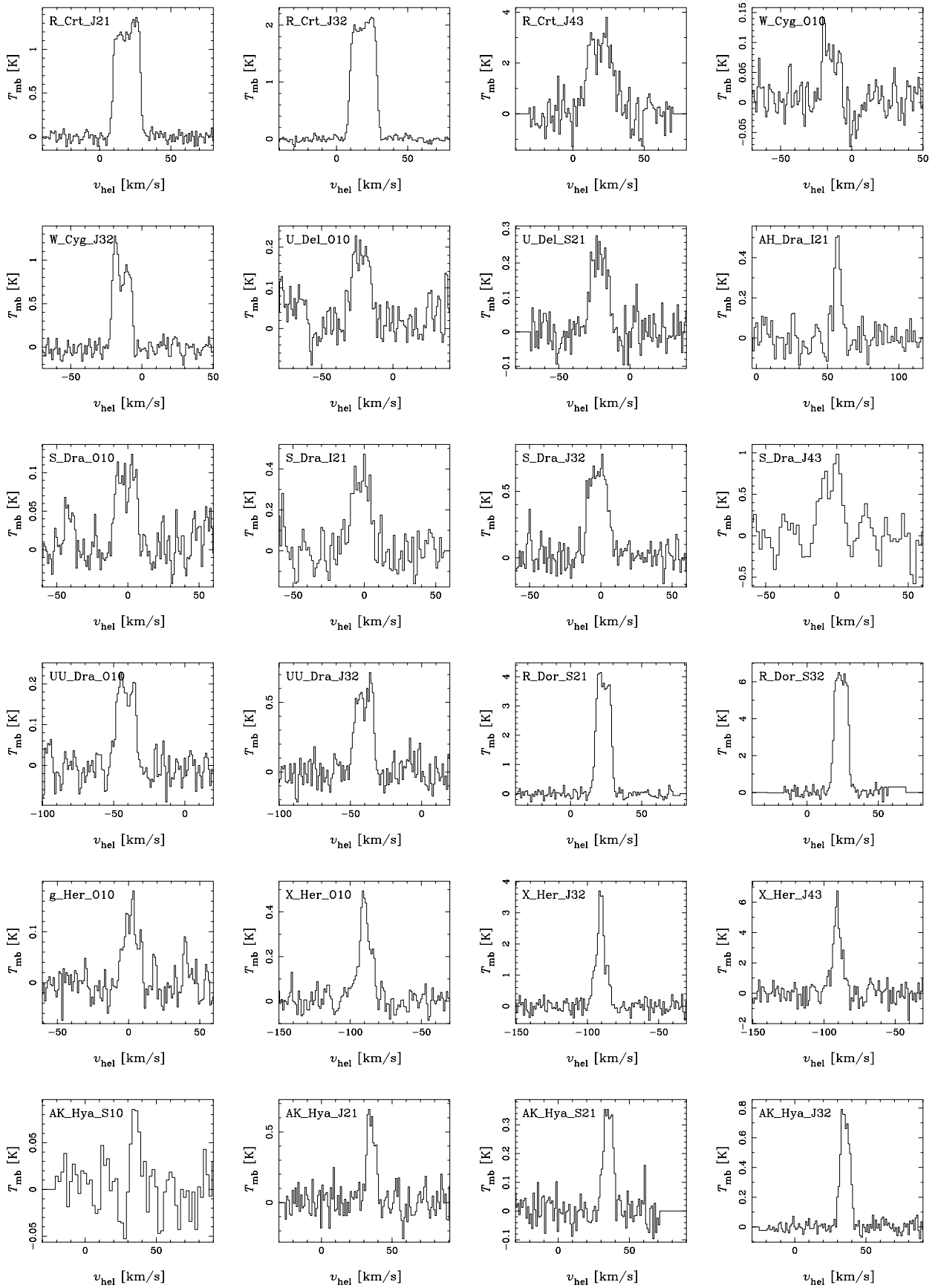


Fig. A4. CO spectra of O-rich SRA and SRb variables (Part 2)

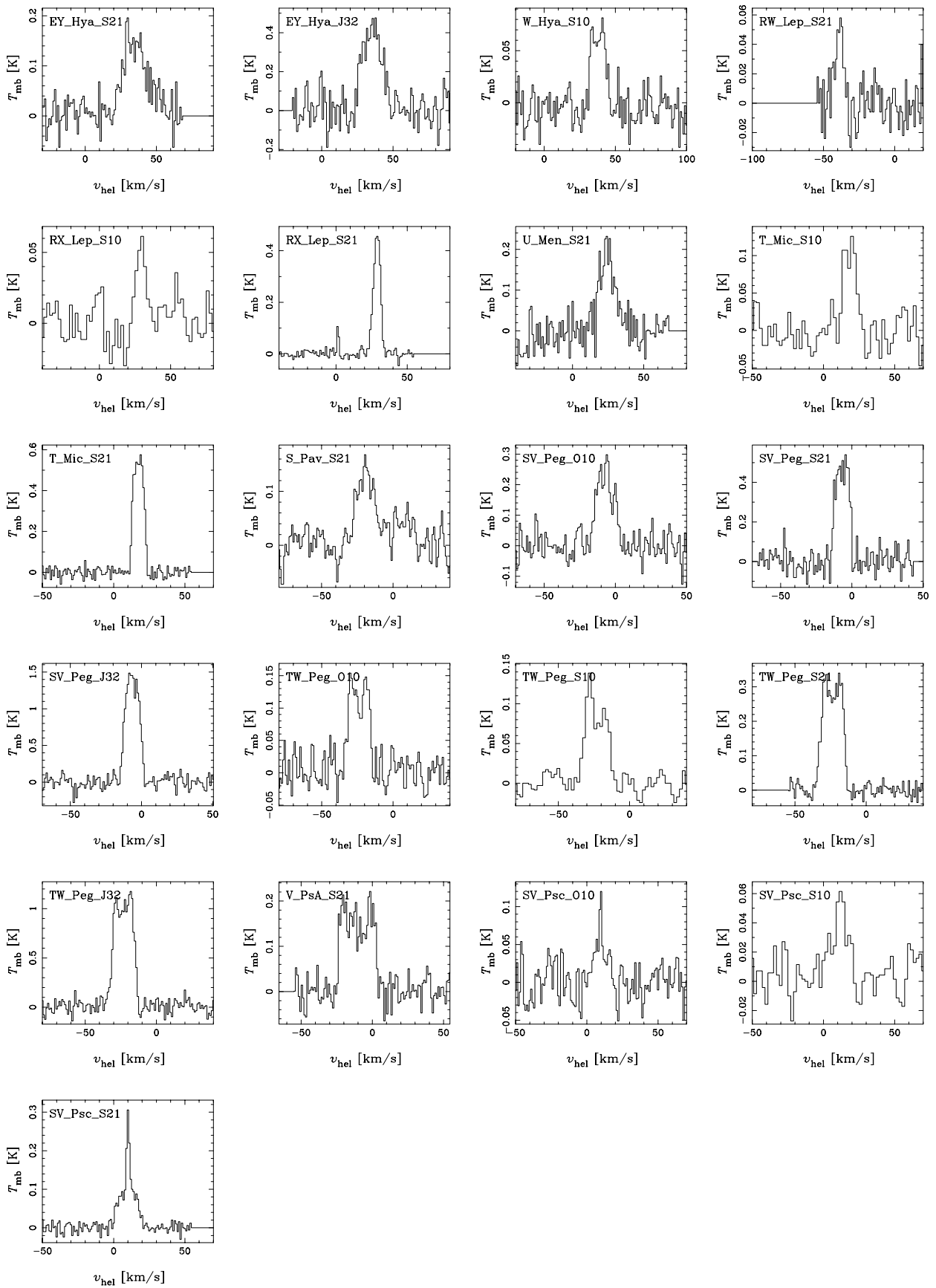


Fig. A5. CO spectra of O-rich SRA and SRb variables (Part 3)

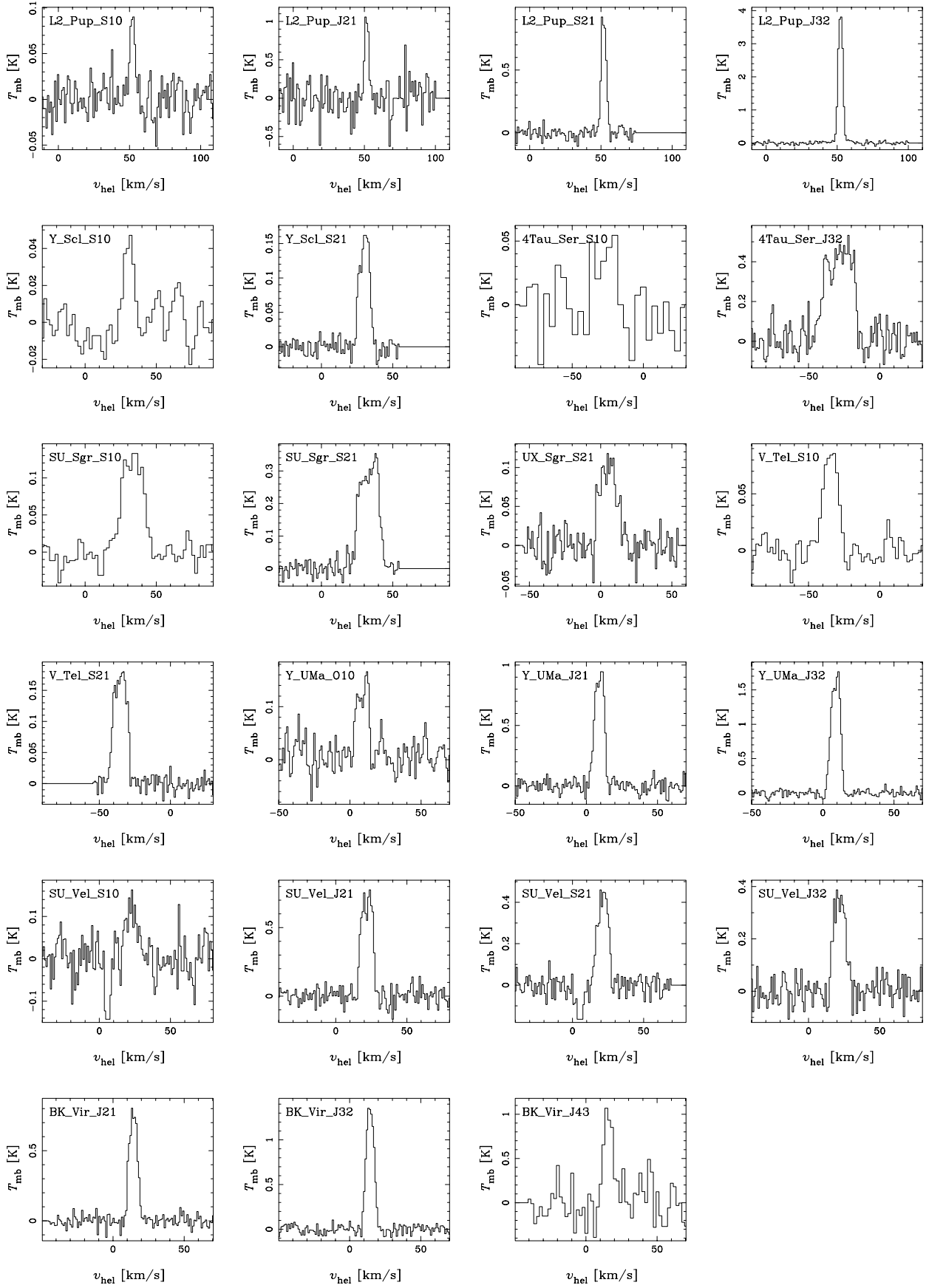
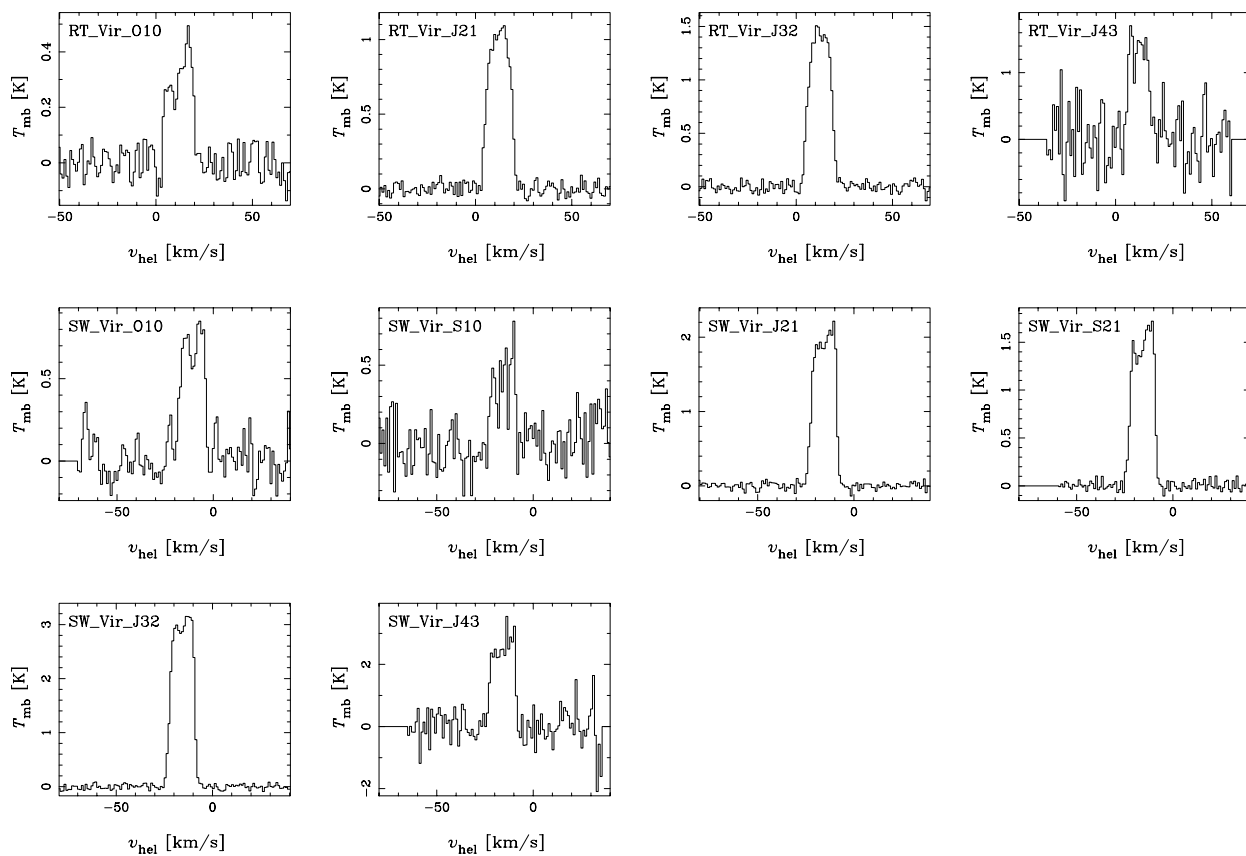


Fig. A6. CO spectra of O-rich SRA and SRb variables (Part 4)



**Fig. A7.** CO spectra of O-rich SRA and SRb variables (Part 5)